



# Seismic Performance Evaluation of Two- and Three-Story Steel Frames with an Upgraded Hybrid Buckling-Restrained Brace

Hesam Azizi<sup>1</sup> · Jamal Ahmadi<sup>1</sup>

Received: 10 June 2024 / Accepted: 4 September 2024  
© The Author(s), under exclusive licence to Shiraz University 2024

## Abstract

A novel hybrid buckling-restrained brace (HBRB) configuration is introduced in this study to address the inherent limitations of conventional buckling-restrained braced frames (BRBFs). The HBRB comprised parallel steel plates with different yield strengths, featuring a low yield point (LYP160) and high strength (SA440B). A staged yielding mechanism is intended to be achieved, whereby the LYP160 cores yield initially during minor seismic excitations while the SA440B core remains elastic, providing requisite re-centering force. The hysteretic behavior of the proposed brace was scrutinized through cyclic loading. Subsequently, pushover and incremental dynamic analyses were conducted on two- and three-story frame models incorporating various bracing configurations to assess seismic performance factors. Furthermore, Nonlinear time history analysis was employed to evaluate the efficacy of HBRBs in mitigating residual displacements. Results indicate that the HBRB exhibits enhanced post-yield stiffness and partial re-centering capacity due to its staged yielding behavior. Comparative pushover and incremental dynamic analysis revealed lower average overstrength and response modification factors for HBRB models obtained from pushover analysis (3.4 and 9.3, respectively) than the incremental dynamic analysis (4.9 and 12.1, respectively). Conversely, a slightly higher ductility reduction factor was observed in the pushover analysis (2.8) relative to incremental dynamic analysis (2.5). Eventually, nonlinear time history analysis demonstrated an average reduction of 18% and 43% in maximum and residual drift ratios for HBRB models compared to BRB models.

**Keywords** Ductility factor · Finite element modeling · Hybrid buckling restrained braced frames · Overstrength factor · Response modification factor

## List of symbols

$V_{eu}$	Elastic design force	$P_y$	Yield force
$V_y$	Yield strength	$P_{max}C$	Maximum axial compressive force
$V_s$	Initial yield level	$\beta$	Ratio of $P_{max,C}$ to $P_{max,T}$
$T$	Natural period	$C_{max}$	Maximum compressive story shear
$R_s$	Actual overstrength coefficient	$K_{inel}$	Inelastic stiffness
$\mu$	Ductility factor	$\Delta_y$	Yield displacement
$\Delta_s$	First plastic hinge	$\Delta_m$	Maximum displacement experienced
$K_1$	Core initial stiffness	$V_y$	Ultimate yield level
$K_2$	Core post-yield stiffness	$\Omega$	Overstrength coefficient
$F_1$	LYP yield strength	$E$	Elastic modulus
$\varepsilon_y$	Yield strain	$\sigma_y$	Yield stress
		$\sigma_u$	Ultimate strength
		$\nu$	Poisson's ratio
		$\varepsilon_u$	Strain corresponding to $\sigma_u$
		$F_2$	HSS yield strength
		$d_1$	LYP yield strength displacement
		$d_2$	HSS yield strength displacement
		$\varepsilon_u$	Ultimate strain
		$P_{max}T$	Maximum axial tensile force
		$\omega$	Ratio of $P_{max,T}$ to $P_y$

✉ Hesam Azizi  
h\_azizi@znu.ac.ir

Jamal Ahmadi  
j\_ahmadi@znu.ac.ir

<sup>1</sup> Structural Engineering Division, Department of Civil Engineering, Faculty of Engineering, University of Zanjan, Zanjan, Iran

$T_{max}$	Maximum tensile story shear
$K_{el}$	Elastic stiffness
$R_{\mu}$	Ductility reduction factor

## 1 Introduction

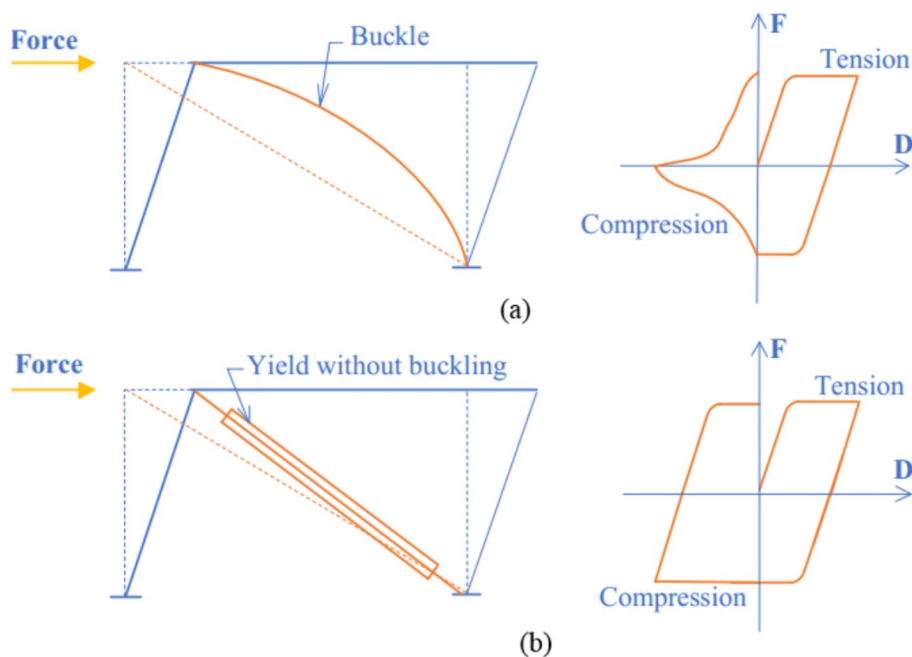
Buckling-restrained braces (BRBs) present a compelling alternative to addressing the inherent limitations of conventional BRBFs by strategically incorporating a core specifically designed to yield under both tensile and compressive forces. This core is meticulously encased within a robust steel sleeve to inhibit buckling during compression. The intervening space between the core and sleeve is then filled with mortar or concrete, providing crucial lateral support and enhancing overall structural integrity (Shen et al. 2017; Kachooee and Kafi, 2018).

The BRB's steel core is engineered to comprise three distinct segments, including the yielding zone, the transition zone, and the connection zone. The yielding zone is designed to absorb and dissipate seismic energy through controlled yielding under tension and compression. This region intentionally possesses a reduced cross-section to ensure localized yielding occurs precisely here, maximizing energy dissipation capabilities. Transverse restraining units constrain the core to preclude global or local buckling of the brace within the plastic region. These restraining units enable the core to yield effectively in compression. The transition zones are flanking the yielding zone on either side, featuring a larger cross-section than the yielding zone. Similar to the yielding zone, the transition zones are also enclosed

by restraining units to maintain structural integrity. Finally, the connection zone outside the enclosed region is crucial to facilitating the seamless connection of the BRB to other structural elements within the frame. Figure 1 compares the hysteretic behavior provided by BRBs and conventional steel braces, highlighting the superior energy dissipation characteristics of BRBs (Zhou et al. 2021).

Several studies, including theoretical (Yakhchalian et al. 2020; Zhao et al. 2016; Wu and Mei 2015), experimental (Khoo et al. 2016; Lin et al. 2012; Jia et al. 2014; Wang et al. 2017a, b), and numerical investigations (Budaházy and Dunai 2015; Tong and Guo 2017; Rahnavard et al. 2018), have been conducted to evaluate the seismic performance of BRBs. Researchers have been working on improving the effectiveness of buckling restrained braces (BRBs) by developing new and innovative designs. These advancements include self-centering BRBs, which minimize post-earthquake structural repair needs by incorporating a self-centering mechanism to address residual deformation (Abou-Elfath 2017). A notable advancement in the field is the development of all-steel BRBs (Bai et al. 2022). These bracing, composed entirely of steel components, significantly enhance post-earthquake recyclability. Additionally, research efforts have been directed towards optimizing the cross-sectional geometry of the BRB core. In this respect, novel designs incorporate I-shaped (Sun et al. 2018; Jiang et al. 2017), H-shaped (Kim et al. 2015), steel angle (Qu et al. 2018; Tong and Guo 2018), and steel tube sections (Hoveidae and Radpour 2021). These cores, readily fabricated from steel members without welding, offer enhanced performance and streamlined manufacturing processes.

**Fig. 1** Comparative hysteresis behavior of conventional steel brace and BRB (Zhou et al. 2021)



Recent investigations have introduced a novel configuration of BRBs exhibiting a double-stage yield behavior. This innovation was achieved through the series and parallel composition of core braces. In the series configuration, Pan et al. (2017) and Sun et al. (2018) proposed the double-stage yielding BRB (DY-BRB), which utilizes smaller and larger cores arranged in sequence. Compared to conventional BRBs, DY-BRBs offer several advantages: they can enter the plastic state during frequent earthquakes, effectively absorbing seismic energy while maintaining the necessary structural stiffness. Additionally, they boast an increased energy dissipation capacity under high-intensity earthquakes (Barbagallo et al. 2019; Yang et al. 2023).

Sugisawa et al. (1995) proposed an alternative approach of BRBs with a core composed of a heterogeneous material combination, including high-strength steel (WT780) and low-yield point steel (LYP100). Laboratory testing of multi-core BRB specimens on 1000-ton machines revealed promising results. Their experiments showed a stable hysteretic behavior and uniform strain distribution up to a loading of 1% axial strain, resulting in the viability of a new BRB design with enhanced energy dissipation capacity through a lower yield point steel core. Atlyan and Charney (2014) proposed hybrid buckling restrained braces (HBRBs), which delved deeper into the behavior of these braces. Their findings confirmed the superior performance of HBRBs across diverse seismic hazard levels, highlighting their ability to reduce permanent drift and mitigate dynamic instability, all while offering cost-effectiveness.

Jia et al. (2018) employed time-history analysis to investigate the seismic response of resilient steel frames equipped with self-centering dual-core BRBs (SC-DBRBs). Their findings demonstrated that SC-DBRBs exhibit superior residual drift performance compared to conventional BRBs with normal-strength steel cores. Similarly, Sitler et al. (2020) proposed a multistage BRB design incorporating parallel cores composed of LYP and high-yield-point steels, resulting in reduced residual drift in BRBs. Heshmati et al. (2022) conducted numerical simulations to assess the application of HBRBs in diagrid structures, revealing substantial improvements in seismic response compared to traditional BRBs. Hu et al. (2022) introduced a two-stage yield BRB design that achieves the desired behavior without the need for parallel dampers or multi-material core plates. Additionally, Azizi et al. (2023) investigated the self-centering mechanism of different yield-strength HBRBs, reporting a stable cyclic response with optimal energy dissipation and self-centering capabilities. In a separate study, Azizi and Ahmadi (2024) proposed a dual-core self-centering buckling restrained brace, demonstrating its effectiveness in mitigating permanent displacements in studied bracing frames. Further research in this domain has been undertaken by various

groups, including the works of Das and Deb (2022), Shi et al. (2023).

Despite their demonstrated effectiveness under various seismic scenarios, a comprehensive understanding of HBRB behavior still needs to be discovered due to several fundamental limitations. Existing research presents a limited characterization of the response modification factor associated with HBRBs. Secondly, the scope of previous investigations has often been restricted to a narrow spectrum of bracing configurations. Eventually, a comprehensive evaluation of the mechanical properties and application limits of steels with different yield strengths concerning meeting the seismic requirements of the existing design codes is imperative for their implementation. Addressing these limitations is imperative to advance the knowledge base and unlock the full potential of HBRBs in earthquake-resistant structural design.

This research has endeavored to enhance the efficiency of HBRB systems by introducing a new configuration characterized by a specialized core arrangement and material selection. A departure from previous studies was undertaken by devising a distinct HBRB configuration designed to mitigate the adverse impacts of steel core interaction, a critical factor influencing the system's performance (Sitler et al. 2020). The proposed brace incorporated a dual-steel core arrangement, wherein plates of differing steel grades were employed in parallel and independent configurations. This design approach effectively eliminated the detrimental S-shaped deformation-induced core interaction. Furthermore, the selection of LYP160 steel for the core addressed the isotropic hardening issues prevalent in lower yield point LYP steels, such as LYP 100, thereby preserving the staged yielding mechanism of the HBRB and preventing a dramatic increase of force in connections and columns (Sitler and Takeuchi 2020). Moreover, the selection of high-strength steel category SA440B was undertaken to mitigate the prevalent high buckling mode characteristic of such steel (Sitler et al. 2020), thereby protecting the local strain capacity of the brace from its adverse impact. Concurrently, a secondary objective was established to comprehensively evaluate the proposed brace's performance, including identifying parameters influencing its seismic response.

To achieve these aims, finite element analysis, incorporating the core-spring technique (Naghavi et al. 2019; Azizi et al. 2023), was employed to investigate the behavior of the proposed model. Hysteretic behavior was initially characterized through cyclic loading, followed by seismic performance assessment via pushover and incremental dynamic analyses conducted on two and three-story frame models featuring various bracing configurations (diagonal, V-shaped, and inverted V-shaped). Seismic performance parameters, such as the response modification factor, were extracted from these analyses. Finally, nonlinear time history

analysis was implemented to quantify the efficacy of HBRBs in mitigating residual drift of braced frames.

## 2 An Overview of Steel Materials

This section highlights steel structures as the dominant choice for multi-story buildings due to their inherent advantages (superior mechanics, prefabrication, fast assembly) (Ban and Shi 2018; SAC 2000; Nakashima et al. 2000). Recent advancements have concentrated on developing high-performance steel (HPS) (Raoul 2005) and introducing innovative structural systems. HPS, enabled by advances in steel production technology (Fukumoto 1996), offers superior strength, weldability, toughness, and corrosion resistance, ultimately improving structural behavior (Raoul 2005). This category includes high-strength steel (HSS), low-yield point (LYP), weathering steel, and more. Conversely, advancements in structural systems target improved seismic performance, faster assembly, self-centering capabilities, reduced carbon footprint, and life-cycle cost efficiency, aligning perfectly with the evolution of HPS structures.

HSS and LYP Steel are highlighted for their desirable qualities in structural engineering. HSS boasts a high minimum yield strength (over 460 MPa), enabling reduced structure weight and member size (Ban and Shi 2018). This point translates to increased space, better aesthetics, design flexibility, and overall efficiency. LYP, while offering a lower yield strength (up to 230 MPa), exhibits exceptional ductility, making it suitable for seismic energy absorption (Bjorhovde 2004; Ban and Shi 2018; Shi et al. 2022, 2019; Yang et al. 2018; Shi et al. 2018a, b). However, as illustrated in Fig. 2, there is a significant difference in their stress–strain behavior. HSS shows a pronounced yield plateau followed by limited ductility, while LYP demonstrates superior ductility but with a lower yield strength (Ban and Shi 2018).

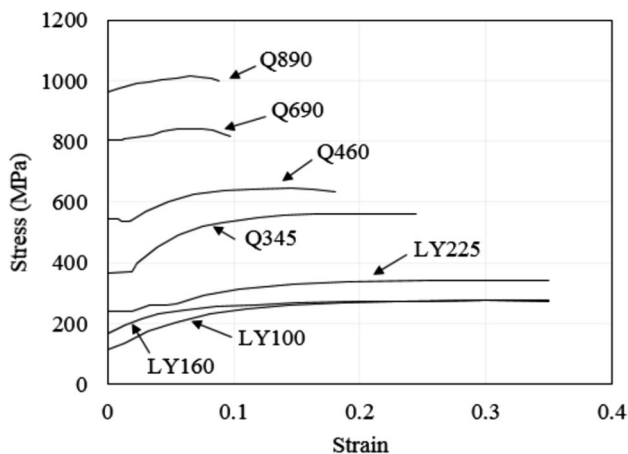


Fig. 2 Typical stress–strain curves of different steels (Shi et al. 2022)

The significantly different material properties of HSS and LYP steels necessitate design adaptations and considerations for seismic performance in structures. Prior research has explored their use in seismic applications: Hu et al. (2017) tested HSS flexural frames, Tenchini et al. (2016) analyzed HSS chevron-braced frames, and Chen et al. (2001) demonstrated good seismic performance of LYP in BRBFs. Established production and standards for both HSS (Shi et al. 2022; Hu et al. 2018; Ban et al. 2012; Bjorhovde 2010) and LYP (Shi et al. 2019; Yang et al. 2018; Shi et al. 2018a, b; Wang et al. 2017a, b; Wang et al. 2016) allow for widespread use. This study investigates the effectiveness of specific HPS types (Sect. 4) in improving the seismic performance of bracing frames, aiming to contribute to HPS-based systems with superior seismic resilience.

## 3 Response Modification Factor

Conventional elastic analysis of structures subjected to seismic excitations often leads to conservative estimates of base shear compared to the actual response witnessed during an earthquake. This phenomenon stems from the inherent ductility of the structure, which manifests as increased resistance beyond the design capacity when the structure enters the inelastic deformation range. This additional strength arises from the fact that the maximum lateral resistance of the structure typically exceeds its design resistance. Consequently, seismic design regulations incorporate this inherent strength and ductility by permitting reduced design loads. The response modification factor ( $R$ ), as detailed in (Asgharian and Shokrgozar 2009), serves as a quantitative measure of the structure's inelastic performance, encompassing its enhanced strength and ductility in the inelastic stage. Figure 3 depicts the typical idealization of the actual nonlinear behavior using a fully bilinear elastoplastic relationship. The

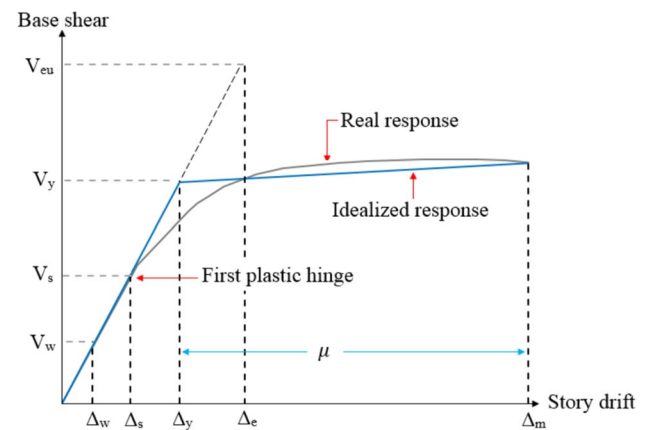


Fig. 3 The general response of the structure (Uang 1991)

yield force ( $V_y$ ) and yield displacement ( $\Delta_y$ ) represent the critical parameters within this representation. Additionally, the Figure highlights the structure's elastic response limit ( $V_{eu}$ ) (Uang 1991).

The building possesses the capacity to dissipate hysteretic energy owing to its ductility. This inherent ability to absorb energy enables the reduction of the elastic design force ( $V_{eu}$ ) to yield strength ( $V_y$ ). The ductility reduction factor ( $R_\mu$ ) is then derived as the ratio of the design load acting on the structure ( $V_{eu}$ ) to the force corresponding to the general yield limit at the onset of failure mechanism formation ( $V_y$ ).

$$R_\mu = \frac{V_{eu}}{V_y} \quad (1)$$

A variety of equations have been proposed for calculating  $R_\mu$ . This work employs the Newmark-Hall equation (Newmark and Hall 1982) for this purpose, as shown below:

$$R_\mu = \begin{cases} \sqrt{2\mu - 1}T \leq 0.5s \\ \mu T \geq 0.5s \end{cases} \quad (2)$$

where  $\mu$  is the ductility factor and calculated as follows:

$$\mu = \frac{\Delta_m}{\Delta_y} \quad (3)$$

$\Delta_m$  is the maximum displacement experienced at the roof level corresponding to the designated performance level, and  $\Delta_y$  is the yield displacement derived from the idealized pushover curve.

The overstrength factor quantifies the inherent reserve resistance of a structure, defined as the difference between its ultimate yield level ( $V_u$ ) and the initial yield level ( $V_s$ ). Mathematically, this relationship can be expressed as:

$$\Omega = \frac{V_u}{V_s} \quad (4)$$

Precise definitions are crucial for overstrength, redundancy, and ductility, which are leveraged to mitigate earthquake forces. This article employs Eq. 2 and the obtained analytical results to compute the frame's overstrength coefficient, denoted by  $\Omega$ . However, the actual overstrength coefficient, denoted by  $R_s$ , employed in R-factor formulations should incorporate additional considerations. Notably, the SEAOC (Uang 1991) framework proposes an overstrength factor for determining the R-factor of BRBFs.

$$R_s = \Omega \times R_1 \times R_2 \times \dots \times R_n \quad (5)$$

Equation 5 introduces the factor  $R_1$  to account for the discrepancy between structural steel's actual and nominal yield strength. Reference (Zhao et al. 2023) suggests a value of 1.05 for  $R_1$ . The  $R_2$  parameter, on the other hand, incorporates the

strain rate effect on yield stress during seismic excitation. Based on the (Zhao et al. 2023) findings, a value of 1.1 can be adopted for  $R_2$  to account for this effect. Consequently, the response modification factor of the structure can be determined using Eq. 6, as illustrated in Fig. 3.

$$R = \frac{V_c}{V_s} = R_\mu \times \Omega \quad (6)$$

In incremental dynamic analysis (IDA), two factors,  $R_s$  and  $R_\mu$ , have been calculated as follows:

The overstrength factor is equal to the ratio of the dynamic base shear, which is responsible for the structure's failure mechanism, to the static base shear, which creates the first plastic hinge in the structure (Mwafy and Elnashai 2002).

$$\Omega = \frac{V_{b(Dyn,u)}}{V_{b(St,y)}} \quad (7)$$

IDA is used to calculate  $V_{b(Dyn,u)}$ . This method increases the utilized earthquake's PGA until the structure reaches the limit state. This PGA that causes the failure mechanism is selected as the ultimate limit state. Then, the base shear of this state is calculated. The pushover analysis was carried out by progressively increasing lateral forces proportional to the fundamental mode shape to obtain the base shear related to the first plastic hinge formation in the structure  $V_{b(St,y)}$  (Fig. 3). This issue means that the ultimate linear limitation of structure in nonlinear static analysis and nonlinear dynamic analysis is considered the same.

The IDA results are directly used to calculate the ductility reduction factor ( $R_\mu$ ) using a linear dynamic analysis according to Eq. (8) (Mwafy and Elnashai 2002).

$$R_\mu = \frac{V_{b(Dyn,el)}}{V_{b(Dyn,u)}} \quad (8)$$

As mentioned, for calculating  $V_{b(Dyn,el)}$ , the PGA, which causes the failure mechanism, is selected as the ultimate limit state, leading to calculating the base shear. For the limit state, the maximum inter-story drift ratio based on the FEMA-351 (2000) is considered to be 3%. Also, performing linear dynamic analysis utilizing this PGA results in the maximum linear base shear. For this purpose, in dynamic analysis, the behavior of structural members is considered in an elastic state. Also, elastic uniaxial material was used to get the linear behavior in Abaqus software instead of uniaxial material.

## 4 General Description

This section introduces the geometric model of HBRB, the materials used in its construction, and the cyclic load specification. Then, the desired steel structures for study are introduced.

## 4.1 HBRB Characteristics

LYP160 was chosen for the LYP core in this investigation. This selection aligns with established practice, as LYP160 is one of three standard materials utilized for BRBs (Zhao et al. 2023). It is characterized by a low yield strength ( $186 \leq \sigma_y \leq 189$  MPa), minimal yield strain, high strain requirement, excellent ductility, moderate overstrength, and negligible isotropic hardening behavior. Also, SA440B was employed for the HSS core. This ductile, high-strength steel exhibits a specified overstrength ratio ( $\sigma_u/\sigma_y \geq 1.25$ ) and fracture elongation ( $\epsilon_f \geq 20\%$ ) (Shi et al. 2018a, b). In contrast to LYP160, SA440B possesses a higher yield strain and lower strain demand (Sitler et al. 2020). It is noteworthy that the yield strength of SA440B ( $440 \leq \sigma_y \leq 540$  MPa) surpasses the upper limit conventionally permitted for seismic members (e.g.,  $\sigma_y \leq 345$  MPa). However, BRBs are exempt from this prescriptive criterion through qualification via physical testing (ANSI/AISC 341–22, 2022).

The proposed HBRB configuration comprises two parallel cores exhibiting distinct yield strengths, as illustrated in Fig. 4. One core, constructed from an LYP160 core plate, functions as an energy absorption element, while the other, comprised of an SA440B core plate, serves as a re-centering member. As depicted, the two cores are spatially segregated.

This study presents a novel configuration characterized by a complete separation between the two cores, a feature distinguishing it from previously investigated geometric models (Sitler et al. 2020; Das and Deb 2022; Shi et al. 2023; Hu et al. 2022; Azizi et al. 2023). This separation eliminates potential adverse interaction between the cores during cyclic loading and S-type deformations. Consequently, implementing non-adhesive materials at the core-concrete interface becomes a viable option. Furthermore, the core plate's maximized length and cross-sectional area obviate the additional welding requirement at the connection zones. The proposed configuration, utilizing hybrid BRB (HBRB) core plates, aims to achieve equivalent total stiffness and

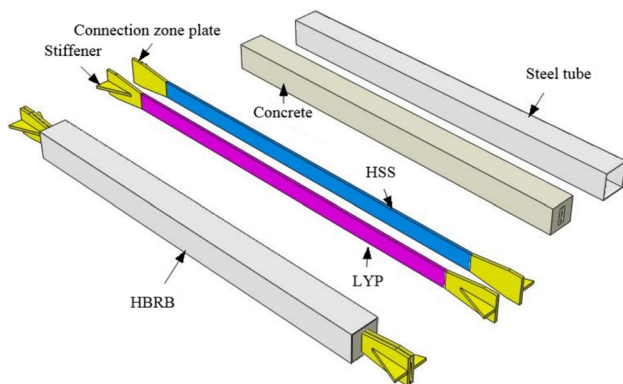


Fig. 4 Details of the proposed geometric model for HBRB

strength to those observed in traditional BRB, enabling a direct and insightful comparison between the two configurations. Under small displacements, the inherent low yield point of the LYP160 core results in the initial yielding of the proposed HBRB mechanism. Conversely, the SA440B core exhibits yielding at larger displacements and under significantly higher forces.

Previous investigations have utilized LYP steels, such as LYP100 (yield strength  $\leq 120$  MPa), with promising results (Sugisawa et al. 1995; Atlayan and Charney 2014; Jia et al. 2018). However, LYP100 exhibits pronounced isotropic hardening ( $\omega$ ), substantially increasing forces acting on bond and column elements in braced frames (Zhao et al. 2023). Furthermore, this material's high strain hardening exponent mitigates the effectiveness of multistage yielding, hindering efforts to significantly reduce residual displacements (Sitler and Takeuchi 2019). Conversely, research frequently employs HSSs such as Q690/HPS100W, characterized by a yield strength exceeding 690 MPa, a yield ratio ( $\sigma_y/\sigma_u$ ) near 0.9, and an ultimate strain below 10% (Sugisawa et al. 1995; Atlayan and Charney 2014; Jia et al. 2018). While these steels offer certain advantages, their utilization may adversely affect the core's higher-mode buckling response and local strain capacity (Sitler and Takeuchi 2020). Therefore, avoiding combinations of steels with substantial discrepancies in yield stress is crucial to achieving the desired stepwise yielding behavior. Based on these considerations, the present study used LYP160 and SA440B steels within the HBRB composition, as they effectively fulfill the criteria above.

## 4.2 Working Mechanism

Within this section, a presentation of the working mechanism and hysteresis model for the introduced HBRB is undertaken.

Figure 5 graphically represents the hysteretic responses of individual members and the overall system subjected to a single cyclic loading. Figure 5a illustrates the hysteresis loop of LYP, which exhibits yielding under relatively low force and consequent energy dissipation. Moreover, LYP's superior ductility enables it to accommodate more significant cumulative plastic deformations (CPD). As shown in Fig. 5b, HSS is characterized by an elevated load-bearing capacity attributed to its higher yield strength. However, its hysteresis loop is comparatively slender due to lower ductility.

Figure 5c illustrates the anticipated behavioral response of the HBRB. Before attaining an external force magnitude  $F_1$ , the LYP and HSS components are maintained in an elastic regime, resulting in a system stiffness denoted as  $K_1$ . Upon exceeding the force threshold  $F_1$ , yield initiation is observed within the LYP core, concentrating plastic

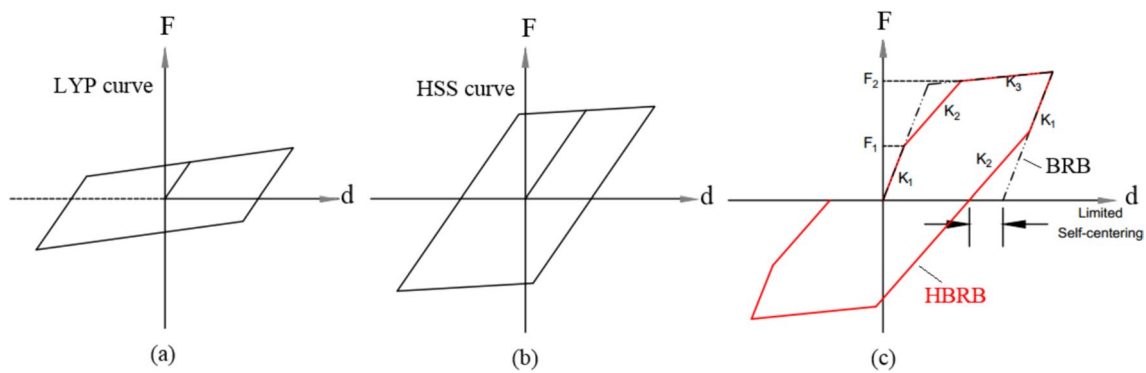


Fig. 5 a, b, and c The idealized hysteretic mechanism of LYP steel, HSS steel, and HBRB, respectively

deformation while the HSS component persists in its elastic state, characterizing the damage-control phase. Notably, the post-yield stiffness ( $K_2$ ) of the HBRB surpasses that of a conventional single-yield-point BRB during this stage. When the external force reaches  $F_2$ , the HSS component yields, assuming the role of a BRB. A BRB exhibiting bilinear kinematic hardening is characterized by an unloading stiffness equivalent to its initial stiffness, leading to a pronounced residual displacement of the steel core component. Conversely, the HBRB, endowed with trilinear kinematic hardening, undergoes premature re-yielding of the LYP steel during reversal loading, facilitating an unloading path converging towards the origin. This phenomenon constitutes the self-centering mechanism intrinsic to the HBRB, resulting in a substantial reduction of residual displacement compared to conventional BRBs.

### 4.3 Case Study Structures

Two previously full-scale tested, two- and three-story laboratory frame specimens were employed in this investigation, as detailed in (Khoo et al. 2016; Lin et al. 2012). Figure 6a depicts the plan and elevation of a representative two-story bay with an 8-m width and a 4-m height. All structural members and BRB cores were fabricated from A572 steel. The second-floor beams were H482 × 300 × 11 × 15 sections, exhibiting yield and ultimate strengths of 414 MPa and 503 MPa in the wing sections and 482 MPa and 538 MPa in the web sections, respectively. The first-floor beams, H488 × 300 × 11 × 18 sections, displayed yield and ultimate strengths of 370 MPa and 486 MPa in the wing sections and 354 MPa and 485 MPa in the web sections, respectively. Both beam types utilized A572 steel with consistent material properties as the first-floor columns (H350 × 350 × 12 × 9). The BRB cores adopted varied cross-sectional areas: 50 cm<sup>2</sup> for the first and 33 cm<sup>2</sup> for the second floors. Their respective yield and ultimate strengths were 372 MPa and 512 MPa for the first floor and 368 MPa and 524 MPa for the second floor.

Gusset plates, with a thickness of 22 mm, were employed as specified in Khoo et al. (2016).

Figure 6b depicts the plan and elevation of a three-story structure with a width of 6 m and a total height of 9.27 m. The structural frame consists of two A992 W12 × 106 columns, W24 × 94 beams for the uppermost floor, and W21 × 68 beams for the first and second floors. The BRBs employ a core cross-section of 15 × 74 mm (1110 mm<sup>2</sup>) and exhibit a yield strength of 383 MPa. All brace plates are fabricated from A572 Grade 50 steel. For a comprehensive elaboration on material properties and design considerations, refer to the research presented in (Lin et al. 2012).

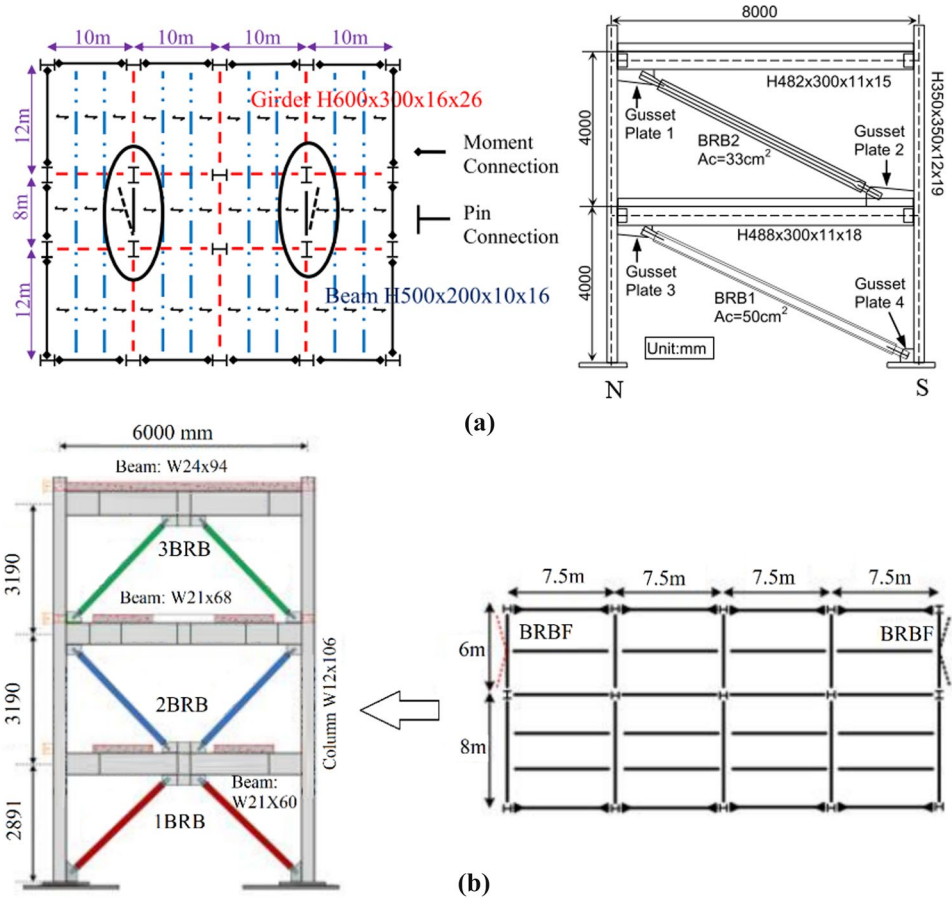
## 5 Numerical Modeling

This section outlines the numerical simulations undertaken to investigate HBRB behavior and that of the corresponding braced frames. Abaqus software was employed for the numerical simulations to leverage the established success of the finite element (FE) approach (Jia et al. 2018; Das and Deb 2022; Azizi et al. 2023).

### 5.1 HBRB Modeling

While meticulously modeling HBRBs in their entirety is technically achievable, it becomes impractical for the current investigation due to two primary factors: computational expense associated with many 3D elements and convergence challenges often encountered with detailed models. Therefore, we adopt a previously validated core-spring finite element model (described in (Rahnavard et al. 2018; Naghavi et al. 2019)) to circumvent the need for constructing a complex model of the entire brace (Fig. 7). This streamlined approach replaces intricate details of concrete, steel casing, and non-adhesive material with spring elements acting orthogonal to the core, effectively preventing buckling. Core-spring modeling involves the external

**Fig. 6** Plan and height of a 2- and 3-story structure (Khoo et al. 2016; Lin et al. 2012), **a** 2-story, **b** 3-story

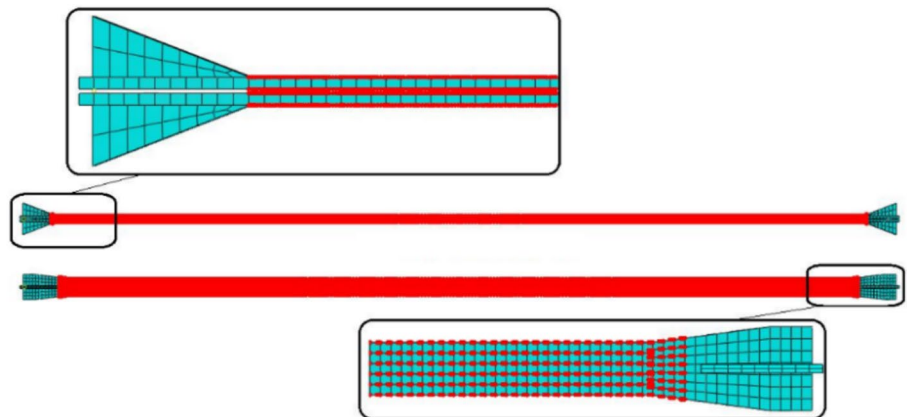


placement of linearly elastic springs at each nodal point of the confining steel cores, substituting conventional restraining member representation. These elements are characterized by substantial deformation capacity, facilitating the investigation of potential steel core buckling phenomena. The methodology entails placing a spring at each nodal point of the confining steel core, situated externally to the core plates. Moreover, springs are introduced

at the existing nodes on the upper and lower flanks of the core plates, oriented transversely.

Spring stiffness determination is contingent upon the mesh discretization and the quantity of springs employed. A spring-based model is subjected to cyclic loading conditions to establish spring stiffness. Iterative adjustment of spring stiffness permits the attainment of hysteresis curves closely resembling the actual model without inducing buckling at the minimum stiffness value. Identical hysteresis curves are

**Fig. 7** Finite element model of core-spring HBRB





subsequently observed upon exceeding this stiffness threshold. Notably, spring placement at specific nodes may be omitted when the steel core discretization is sufficiently fine, resulting in a buckling load surpassing the core yield stress.

To accurately represent the behavior of BRBs and HBRBs, the cores, end connections, and stiffeners were modeled using octahedral solid elements with reduced integration (C3D8R). Furthermore, an initial displacement, equating to 0.001 times the core length, has been considered perpendicular to the midpoint of the brace length axis to account for the influence of imperfection. As depicted in Fig. 7, the finite element model incorporates a core-spring model as an alternative to the restraining members typically employed within HBRB cores.

This investigation studies the influence of material properties on HBRB performance by utilizing two distinct steel alloys possessing varying yield stress values. A nonlinear kinematic hardening model, previously established within FE software, was incorporated for the numerical simulation. Prior studies have substantiated the effectiveness and accuracy of this combined approach (Jia et al. 2018; Azizi et al. 2023). Material parameters pertinent to the nonlinear models were procured from the existing literature. The mechanical properties of the steels are presented in Table 1.

The displacement loading protocol outlined in ANSI/AISC 341–22 (2022) was employed (Fig. 8a) to investigate the cyclic performance of braces.  $\Delta_y$  represents the displacement corresponding to the yielding of the LYP160 core plate, while  $\Delta_{bm}$  signifies the axial brace deformation corresponding to the design story drift. As per AISC guidelines,  $\Delta_{bm}$  was determined based on a story drift of 0.02 (Fig. 8b). The corresponding calculated value of  $\Delta_{bm}$  aimed to achieve a cumulative inelastic displacement (CID) of 200. This study chose an  $\Delta_{bm}$  value of 70 mm, enabling the models to exceed the target CID of 200.

## 5.2 Structural Modeling

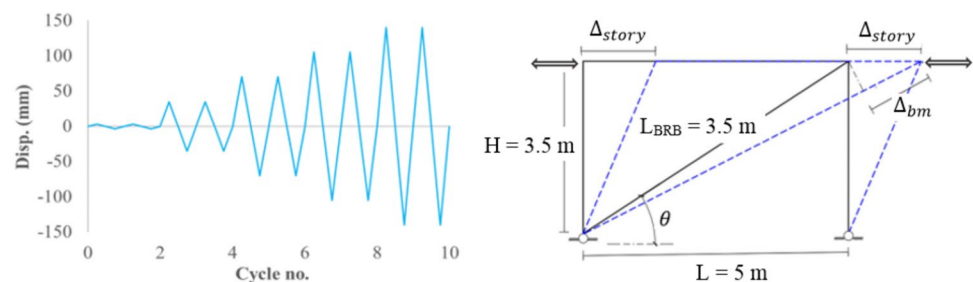
This study utilized the four-node, six-degree-of-freedom linear element (S4R) with reduced integration within FE software to model diverse components of braced frames such as core plates, encompassing bracing frames, gusset plates, end connections, stiffeners, beams, and columns. Since welding is the predominant joining method, tie constraints were employed to establish connections between bracing members and connection sections, stiffeners and connections, connections and end rectangular plates, and beams and columns. After conducting previous investigations (Naghavi et al. 2019; Azizi et al. 2023) and performing sensitivity analysis, a uniform mesh size of approximately 50 mm was implemented to the beams, columns, and the core of the braces. This choice was made to balance between computational efficiency and model accuracy. Conversely, a finer mesh size of 30 mm was adopted for gusset plates and the member connection regions. For all models, quadrilateral (Quad) elements and a structured meshing technique were consistently employed to guarantee mesh compatibility, enhance modeling accuracy, and mitigate the potential for non-convergence errors.

The researchers used 2- and 3-story frames with different floor spans and heights, previously described by Khoo et al. (2016) and Lin et al. (2012). The study analyzed a total of eight two-story frames and eight three-story frames. Each set included four frames with buckling-restrained braces (BRBs) and four with HBRBs. The HBRBs were arranged in diagonal, V-shaped, inverted V-shaped (IV-shaped), and double-X (2X) configurations, while the BRBs were configured in diagonal, zigzag, V-shaped, and IV-shaped arrangements. Model nomenclature is established through a two-part system. Initially, a hyphenated abbreviation denoting the bracing frame arrangement type is assigned. Subsequently, the prefix “HBF” is appended for hybrid models,

**Table 1** Materials mechanical properties

Steel grade	$\sigma_y$ (MPa)	$\sigma_u$ (MPa)	$\epsilon_u$	E (GPa)	$\nu$	References
A572 G.50	345	485	0.198	186.2	0.300	(Azizi et al. 2023)
SA440B	505	653	0.100	205.0	0.300	(Sitler et al. 2020)
LYP160	160	270	0.271	198.6	0.285	(Shi et al. 2018a, b)

**Fig. 8** a AISC cyclic loading; b Frame used for loading protocol determination



incorporating the first two letters of “HBRB” and the initial syllable of “frame”. Conversely, the prefix “BF” is utilized for BRB models, comprising the first letter of “BRB” followed by the initial syllable of “frame”. For instance, “IV-HBF” represents HBRBF with an IV bracing configuration, while “Z-BF” identifies a BRBF model featuring a zigzag bracing arrangement.

This study adheres to established US design recommendations, as outlined in references (Khoo et al. 2016; ANSI/AISC 341–22, 2022; SAC 2000; ASCE/SEI 7–22, 2022; SEAOC 2021). Building upon a prior study (Naghavi et al. 2019), two-story frame models were analyzed and designed under identical conditions. These models were assumed to reside on soil type I. Both story force distribution and displacement-based procedures, documented in (Khoo et al. 2016), were employed in the building design. The design dead load (DL) and live load (LL) were set at 6.89 kN/m<sup>2</sup> and 2.45 kN/m<sup>2</sup>, respectively.

Following the structural engineers association of California (SEAOC) guidelines (SEAOC 2021), a response modification factor (*R*) of 8 was adopted for the models. Beam-to-column connections were assumed to be pinned at both ends, as the frames were not designed for moment resistance. Additionally, the braces were configured to withstand 100% of the lateral load. The BRBs were designed according to the seismic provisions outlined in ANSI/AISC 341–22 (2022). While previous tests indicated a 10% higher compression strength than tension strength (SAC 2000), this study assumes equal strengths for both. The frame member dimensions across various configurations were governed by those specified in (Khoo et al. 2016), effectively meeting the requirements for all models. Since the initial stiffness and strength of the hybrid BRBs are maintained at the same level as traditional BRBs, they inherently adhere to capacity design principles. Consequently, no additional effort is required to create code-based design rules for hybrid BRBFs (as referenced in Atlayan and Charney 2014).

Three-story models were designed and experimentally investigated under conditions replicating those employed in the research presented by (Lin et al. 2012). These three-story frame models were intended for construction in Los Angeles. A uniformly distributed design dead load of 7.35 kN/m<sup>2</sup> and a reduced live load of 1.22 kN/m<sup>2</sup> were assumed for the floor slabs. As mandated by the seismic building requirements outlined in (Chen et al. 2001), the design base earthquake was associated with an elastic spectral acceleration of 1.07 *g*. Based on a numerical model analysis, the fundamental period of the structure was determined to be 0.603 s. Utilizing an importance factor of *I* = 1.0 and a response modification factor of *R* = 8, the design base shear force was calculated to be 618 kN. Following a comprehensive selection process, six BRBs were chosen, each possessing an identical core cross-sectional area of 1110 mm<sup>2</sup>

(74 × 15 mm<sup>2</sup>) and a yield strength of 383 kN. Under the design base shear of 618 kN, the two BRBs in the first story were anticipated to resist approximately 80% of the total shear force and reach nearly 90% of their yield strength in tension and compression. Two-story models, adhering to the dimensional specifications outlined in (Lin et al. 2012), demonstrated seismic compliance across diverse configurations.

### 5.3 Model Validation

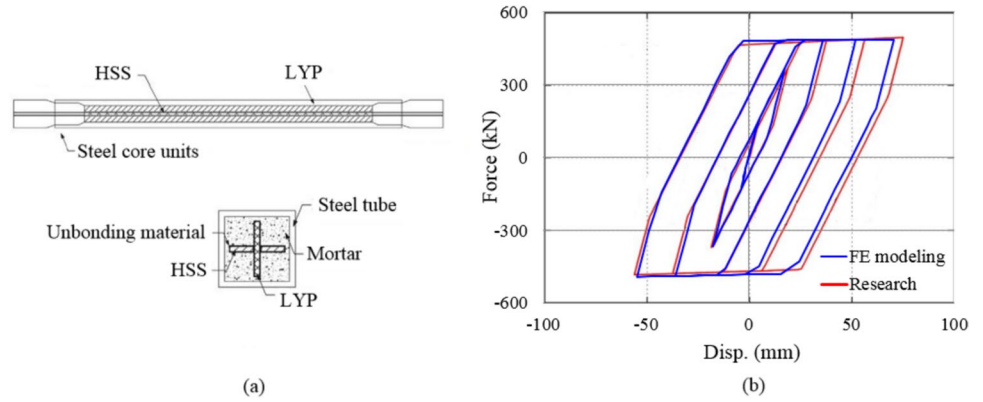
In this section, the validation of the numerical methods employed in HBRB and BRB modeling was performed by employing the results of four conducted research in the literature (Jia et al. (2018), Sitler et al. (2020), Khoo et al. (2016), Lin et al. (2012)). In this respect, a comparative analysis is conducted between the force–displacement values garnered from studied models and those documented in prior studies. Notably, Jia et al. (2018) undertook a theoretical and numerical investigation on self-centering dual BRB (SC-DBRBs) incorporating Q690 and Q100 steel cores, characterized by nominal yield strengths of 690 MPa and 100 MPa, respectively. The cores above possessed identical cross-sectional areas of 600 mm<sup>2</sup> and were configured in a parallel arrangement reminiscent of a sandwich-like cross-section (Fig. 9a). The spring stiffness of the SC-DBRB cores was experimentally characterized by applying a range of loading values. The corresponding cyclic responses are presented in Fig. 9b. As illustrated in Fig. 9b, a high degree of agreement is observed between the experimental results and the finite element (FE) modeling, demonstrating the method’s accuracy.

Figure 10 depicts the Von Mises stress distribution contour within the SC-DBRB finite element model. Notably, the transition and connection zone of SC-DBRB exhibits considerably lower stress levels. This attenuation is attributed to the implementation of larger sections and the incorporation of stiffeners. Furthermore, the cores display a uniform stress distribution, reflecting the inherent properties of their material composition.

Leveraging the findings of Jia et al. (2018), the parameters were calibrated, whose values are presented in Table 2. The numerical modeling yielded parameters exhibiting slight discrepancies from prior research (Jia et al. 2018). These discrepancies may indicate limitations in the model’s ability to capture the underlying physical phenomena accurately.

Building upon the work of Sitler et al. (2020), this study investigates the cyclic behavior of a multistage buckling-restrained brace (MS-BRB) through small-scale specimen testing. The MS-BRB incorporates a unique core configuration comprised of three rectangular plates welded together in a cruciform pattern (Fig. 11a). These plates, designated LY225, boast short yield lengths and a yield strength range

**Fig. 9** Study conducted by Jia et al. (2018): **a** details of SC-DBRB; **b** comparison between FE modeling and empirical results



**Fig. 10** Von Mises stress distribution contour, **a** SC-DBRB model, **b** MS-BRB model

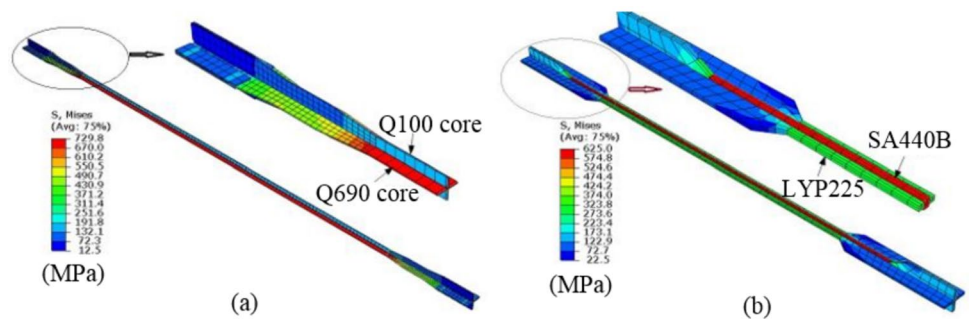
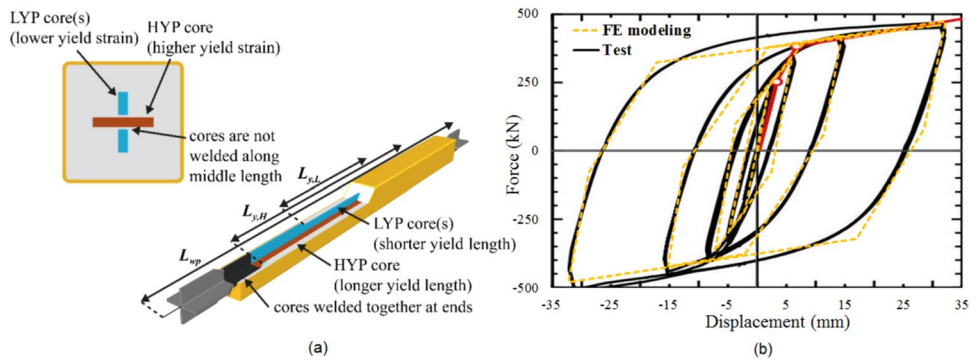


**Table 2** Comparison of results from FE modeling and previous studies

Research	$F_1$ (kN)	$d_1$ (mm)	$F_2$ (kN)	$d_2$ (mm)	$K_1$ (kN/mm)	$K_2$ (kN/mm)
Jia et al. (2018)	120	3.65	478	24.82	33.86	17.10
FEM (current study)	120	3.65	476	25.11	32.92	16.55
Difference (%)	0.00	0.00	0.42	-1.16	2.78	3.22
Sitler et al. (2020)	251.0	2.90	384.0	6.30	87.0	39.15
FEM (current study)	260.3	3.03	384.7	6.15	84.0	41.11
Difference (%)	-3.71	-4.48	-0.18	2.38	3.50	-5.00

**Fig. 11** Experimental test by Sitler et al. (2020): **a** details of MC-BRB specimen; **b** comparison between FE modeling and experimental measurements



of  $205 \leq f_y \leq 245$  MPa. Notably, a single high-yield point (HYP) core, designated as SA440B, is strategically incorporated into the design. This HYP core features a longer yield length and a yield strength range of  $440 \leq f_y \leq 540$  MPa. The separation of the plates along their midsection differentiates

this design from conventional BRBs, potentially influencing its mechanical response. Figure 11 and Table 2, respectively, illustrate the comparative hysteresis response and its associated parameters. In this case, the FE modeling results strongly concord with the experimental test data, further

supporting the model’s validity. Figure 11b depicts the Von Mises stress distribution contour of the MS-BRB finite element model. Notably, the MS-BRB transition and connecting regions exhibit markedly lower stress levels than the cores. Furthermore, the stress within the cores exhibits a uniform distribution along their longitudinal axis.

Furthermore, this study uses the laboratory frames described in the preceding section as the foundation for another model validation. The numerical model depicted in Fig. 12, representing a two-story braced frame with the general characteristics outlined previously, served as the basis for generating the hysteresis curve. Figures 12b and 13a illustrate the Von Mises stress contour and a comparison of the hysteresis responses obtained through numerical analysis and laboratory testing. Figure 12b demonstrates the model’s accuracy by depicting the frame’s BRBs yielding before the primary members, signifying their role as sacrificial elements. Furthermore, Fig. 13a reveals a close correspondence between the hysteresis responses acquired from

numerical analysis and laboratory measurements, solidifying the model’s validity.

Table 3 presents the comparative analysis of numerical and experimental data. It delves into a detailed comparison of key cyclic response parameters, including  $V_y$ ,  $C_{max}$ ,  $T_{max}$ ,  $K_{el}$ , and  $K_{inel}$ , as extracted from the corresponding numerical and experimental hysteresis curves. Notably, the results exhibit close agreement between those reported by Khoo et al. (2016) and the current numerical simulations.

Further validation of the numerical modeling approach comes from the laboratory experiment conducted by Lin et al. (2012). This study investigated the behavior of a frame system incorporating BRBs. The modeling process employed the two-story frame design detailed earlier (refer to Chen et al. 2001 for specifics of the laboratory frame). Figure 14 depicts the finite element model alongside the corresponding von Mises stress contour. As anticipated by the design, the BRBs, possessing a smaller cross-sectional area, exhibited greater stress concentration and plastic

Fig. 12 a Finite element model produced based on (Khoo et al. 2016), and b Von Mises stress contour of the model

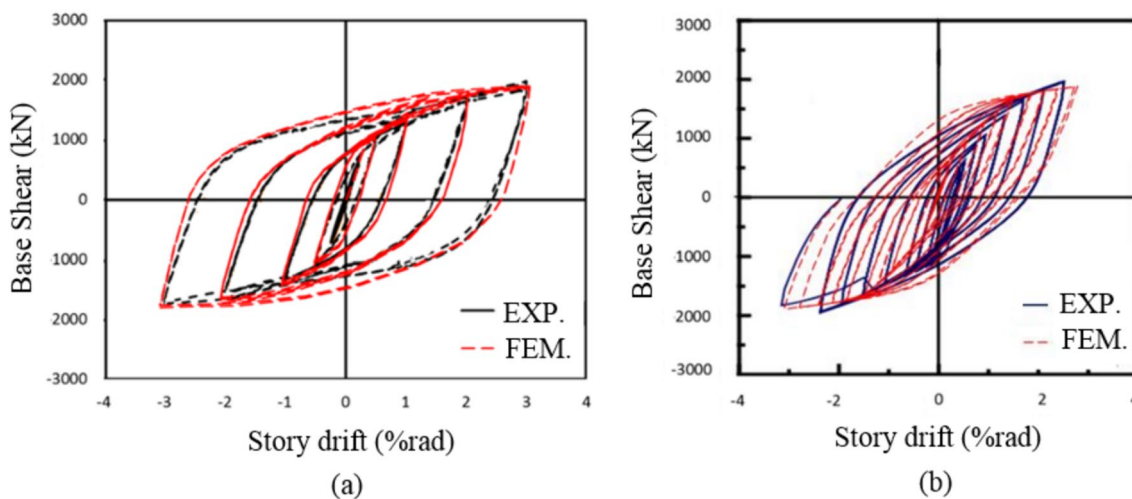
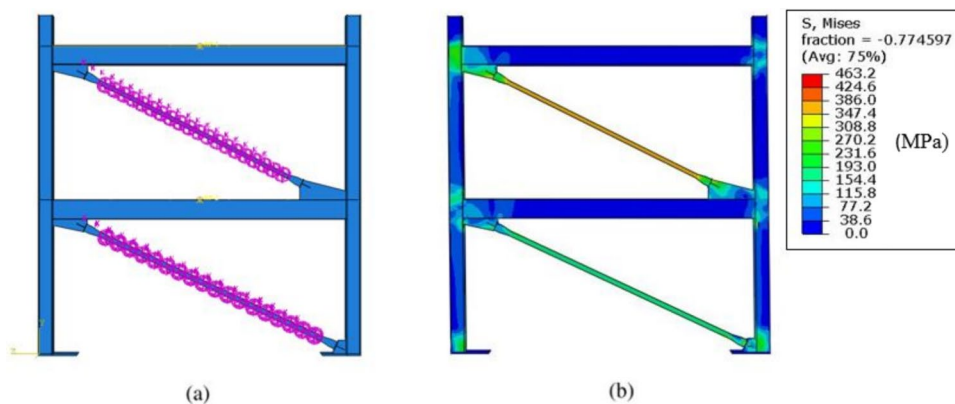


Fig. 13 Hysteresis curves obtained from a test specimen (Khoo et al. 2016), b test specimen (Lin et al. 2012)

**Table 3** Comparison between the results calculated from the FE modeling and obtained from tests

Case		Frames					Related brace						
		$V_y$	$T_{max}$	$C_{max}$	$K_{el}$	$K_{inel}$	$\varepsilon_y$ (%)	$\varepsilon_u$ (%)	$P_y$	$P_{max,T}$	$P_{max,C}$	$\omega$	$\beta$
1	Khoo et al. (2016)	1242	1886	1748	347.80	31.20	0.18	1.70	1350	1411	1654	1.05	1.17
	FEM (This study)	1273	1890	1749	351.20	30.10	0.20	1.70	1382	1443	1695	1.04	1.17
	Difference (%)	2.49	0.22	0.09	0.98	-3.52	11.11	0.00	2.37	2.27	2.48	-0.10	0.21
2	Lin et al. (2012)	1604	1827	1979	168.10	16.80	0.18	4.00	383	616	824	1.61	1.34
	FEM (This study)	1530	1846	1886	174.50	17.50	0.20	4.00	396	631	792	1.59	1.26
	Difference (%)	-4.48	1.02	-4.71	3.81	4.16	11.11	0.00	3.39	2.44	-3.88	-0.93	-6.17

deformation than the remaining primary frame members. Figure 13b compares the experimental and numerical hysteresis curves, revealing substantial agreement in the cyclic response parameters, particularly the peak tensile forces. Table 3 compares these parameters, demonstrating that the discrepancies between the numerical and experimental values fall within a margin of 5%.

Comparison of experimental results with finite element analysis demonstrates the high accuracy of the developed modeling method. This accuracy empowers the model to generate highly accurate response predictions within the scope of parametric studies.

## 6 Analysis and Results

This section presents the results obtained from analyses conducted on the studied models. These encompass cyclic loading, pushover, incremental dynamic, and time history analyses.

### 6.1 Cyclic Response of HBRB

To elucidate the intricacies of local responses and enable direct comparisons, two distinct braces, a conventional BRB and a novel HBRB, were meticulously modeled and subsequently analyzed.

Figure 15 presents the hysteresis curves for the HBRB and the BRB specimens. Figure 16 subsequently illustrates the distribution of Von Mises stress and equivalent plastic strain (PEEQ), a measure of material plasticity within the specimens.

An initial parity in stiffness ( $K_1$ ) is observed between the two brace types. However, the HBRB exhibits a demonstrably higher post-yield stiffness ( $K_2$ ) than the BRB. This enhanced post-yield characteristic is advantageous, as evidenced by references (Jia et al. 2018; Sitler et al. 2020; Azizi et al. 2023), by impeding the formation of a weak story phenomenon within braced frames subjected to lateral loads. In contradistinction to the bilinear behavior exhibited by the BRB, the HBRB demonstrates an incremental trilinear kinematic hysteresis response attributable

**Fig. 14** a Finite element model produced based on (Lin et al. 2012), b Von Mises stress contour of the model

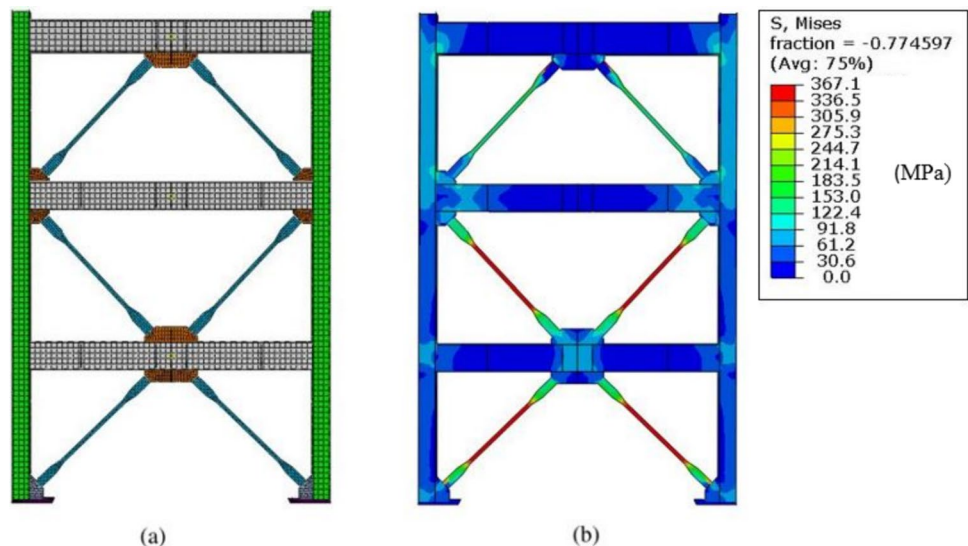


**Fig. 15** Hysteresis responses of models

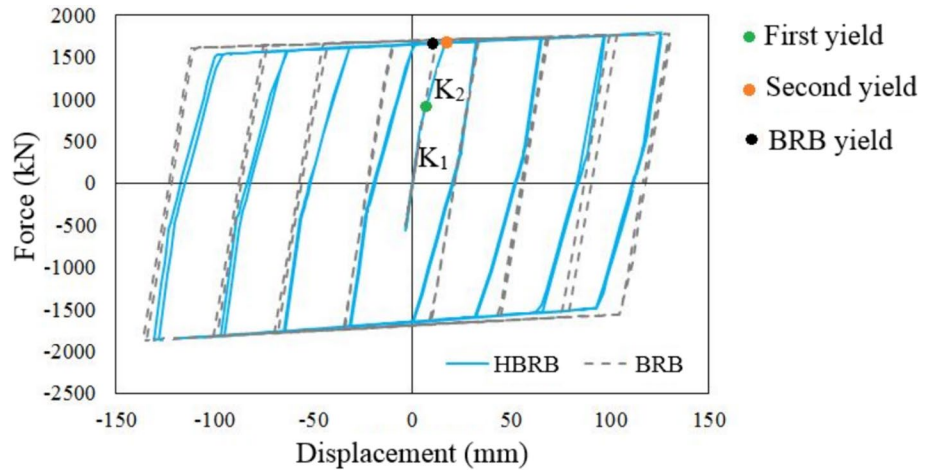
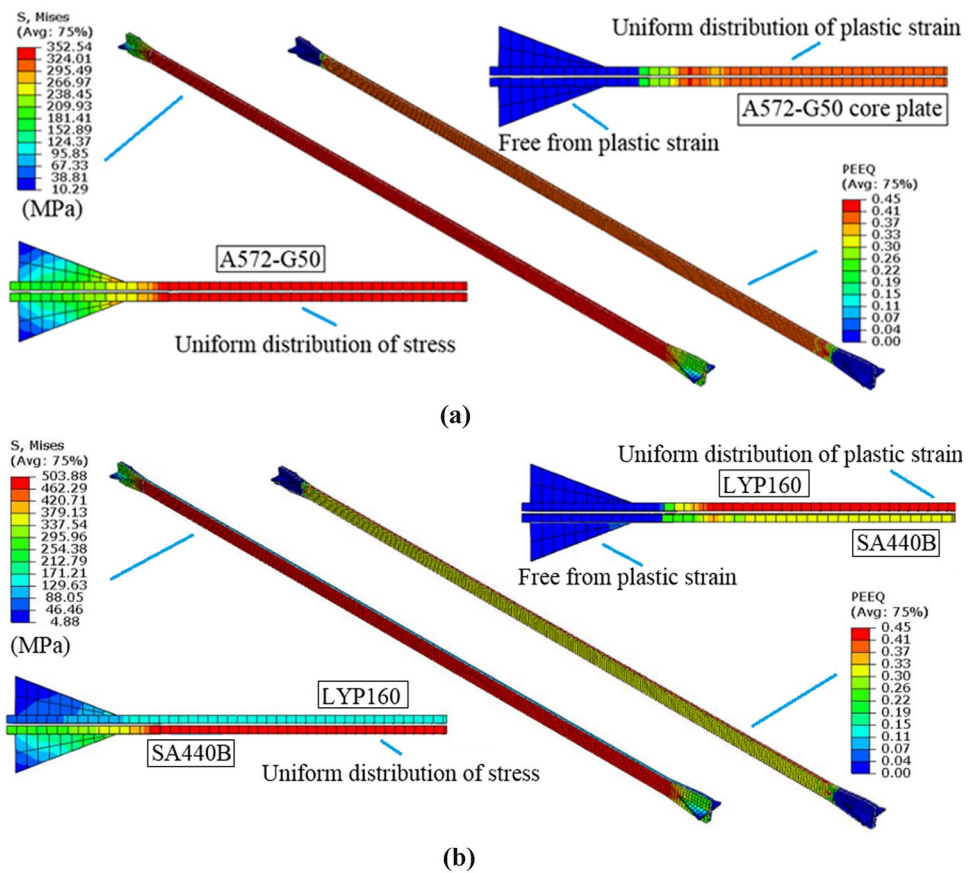


**Fig. 16** Von Mises stress and PEEQ distribution: a BRB, b HBRB



to its possession of two distinct yield points. Consequently, a staged response with a relative re-centering property is observed during unloading cycles. This behavior is anticipated to reduce the permanent displacement experienced by the HBRB compared to the BRB. Therefore, compared to the BRB, the HBRB exhibits significantly reduced residual displacement, reaching 54%, 36%, 24%, and 17% lower values under the  $\pm 0.5\Delta_{bm}$ ,  $\pm \Delta_{bm}$ ,  $\pm 1.5\Delta_{bm}$ , and  $\pm 2\Delta_{bm}$  cycles, respectively. It worth noting that in this research, similar to

studies (Jia et al. 2018; Shi et al. 2022; Chen et al. 2023), unloading lines in hysteresis curves were used to investigate the reduction of residual displacement. This enhanced performance is attributed to the HBRB's lower initial yield strength than the BRB, allowing it to reach the yield point more readily and enter the plastic stage to dissipate seismic energy effectively. This favorable characteristic is primarily due to the use of LYP160 steel.

To elucidate the mechanisms behind the observed reduction in permanent displacements, we present comparative contours of the PEEQ for the cores in the final loading cycle (Fig. 16). The Figure shows that the LYP160 core exhibited more extensive inelastic deformations than the A572 core, attributable to its earlier yielding behavior. Conversely, the SA440B core displayed limited plasticity due to its high elastic range, leading to a partial re-centering phenomenon observed in the unloading cycles of its hysteretic response. A detailed examination of the von Mises stress, and PEEQ contours can provide further insights into these observations.

## 6.2 Pushover Analysis

Considering its ability to predict the inelastic force–deformation behavior of structures, nonlinear static analysis employing pushover methods has become a widely adopted technique (Atlayan and Charney 2014; Asgarian and Shokrgozar 2009; Newmark and Hall 1982). This approach offers a straightforward yet insightful understanding of the anticipated structural response. This study’s pushover analysis employs a control location corresponding to the dominant lateral deformation mode, with a maximum frame period of 0.03 radians. Pushover curves are generated until the target point is reached. Subsequently, capacity curves are constructed for each structure, and behavioral parameters are extracted by equivalently representing these curves as bilinear diagrams. The relationship between base shear and roof displacement is determined for various bracing configurations and frames with differing floor numbers. The two-story models’ rotation time and final displacement reach 0.24 s and 240 mm, respectively. These values increase to 0.27 s and 290.5 mm for three-story models.

### 6.2.1 Plasticity of the Models

The contour lines of the plastic strain distribution at various loading stages were extracted and presented for 3-story models to facilitate a comprehensive evaluation of the plasticization process within the members. These stages encompassed the onset of yielding for LYP160 and SA440B materials and applied displacements of 0.01, 0.02, and 0.03 radians. Incremental displacement loads were imposed, with element plasticity being computed at each loading step. The plastic behavior of the BRBF and HBRBF models under these differing loading conditions is graphically illustrated in Fig. 17 and Fig. 18.

Notably, within the context of HBRBF models, the frame’s frontal and rear view representation has been employed to visualize the distribution of plastic strain contours in steel cores (LYP160 and SA440B). Consequently, the images of both the frontal and rear sides are presented for

all bracing configurations. These visualizations are provided for various loading stages, commencing the core yielding and applied displacements up to 0.01, 0.02, and 0.03 radians. In contrast, owing to using a single steel grade (A572) in the core of BRBFs, the presentation of analysis outputs is restricted to a singular view.

A review of Figs. 17 and 18 reveals that the gusset plates exhibit no evidence of plasticity, suggesting the adequacy of the gusset plate design requirements employed in the models. As anticipated, yielding was initiated in BRBF models through the yielding of the A572 core plate, while in HBRBF models, yielding commenced with the yielding of the LYP160 core plate. Moreover, brace yielding progressed sequentially from the second to the third and subsequently to the first floor.

Comparative analysis of the PE distribution contours of BRBF and HBRBF model members, as depicted in Figs. 17 and 18, indicates a higher degree of plasticity in BRBF members, particularly at rotation angles of 0.02 and 0.03 radians, relative to HBRBF members. This phenomenon is attributed to the LYP160 core in HBRB models, which, due to its early yielding and substantial energy dissipation capacity, effectively inhibits the plastification of primary members. Furthermore, Figs. 17 and 18 demonstrate the absence of plastic hinge formation in both BRB and HBRB, owing to the buckling restraint provided by the restraining units. Also, it is observed that within both bracing systems, BRB and HBRB, under varying load conditions, the diagonal model exhibits a lesser degree of plasticity than other models. Nevertheless, the lower PE values observed at the column extremities of IV models compared to V and diagonal models contribute to preventing structural instability in these models.

### 6.2.2 Idealization of Pushover Curve

In order to facilitate the analysis of the results, an elastic–plastic idealization of the load–displacement ( $V$ - $\Delta$ ) behavior was adopted in Fig. 3. The identification of two key points characterizes this bilinear representation. The first is the effective yield displacement ( $\Delta_y$ ), which signifies the transition from elastic to plastic behavior. The second is the ultimate displacement ( $\Delta_u$ ). These idealized diagrams were derived from their analytical counterparts using the method based on balanced energy (MBBE) (Lam et al. 2003). Within this method, the idealization process ensures that an energy equivalence is achieved between the analytical curve and the idealized bilinear diagram. This issue is accomplished by equating the area under the analytical curve to the area under the ideal elastic–plastic curve. Ultimate displacement is the point in the descending branch of the load–displacement curve where the load reaches 85% of its peak value (Wang and Hsu 2001). For models that lack a

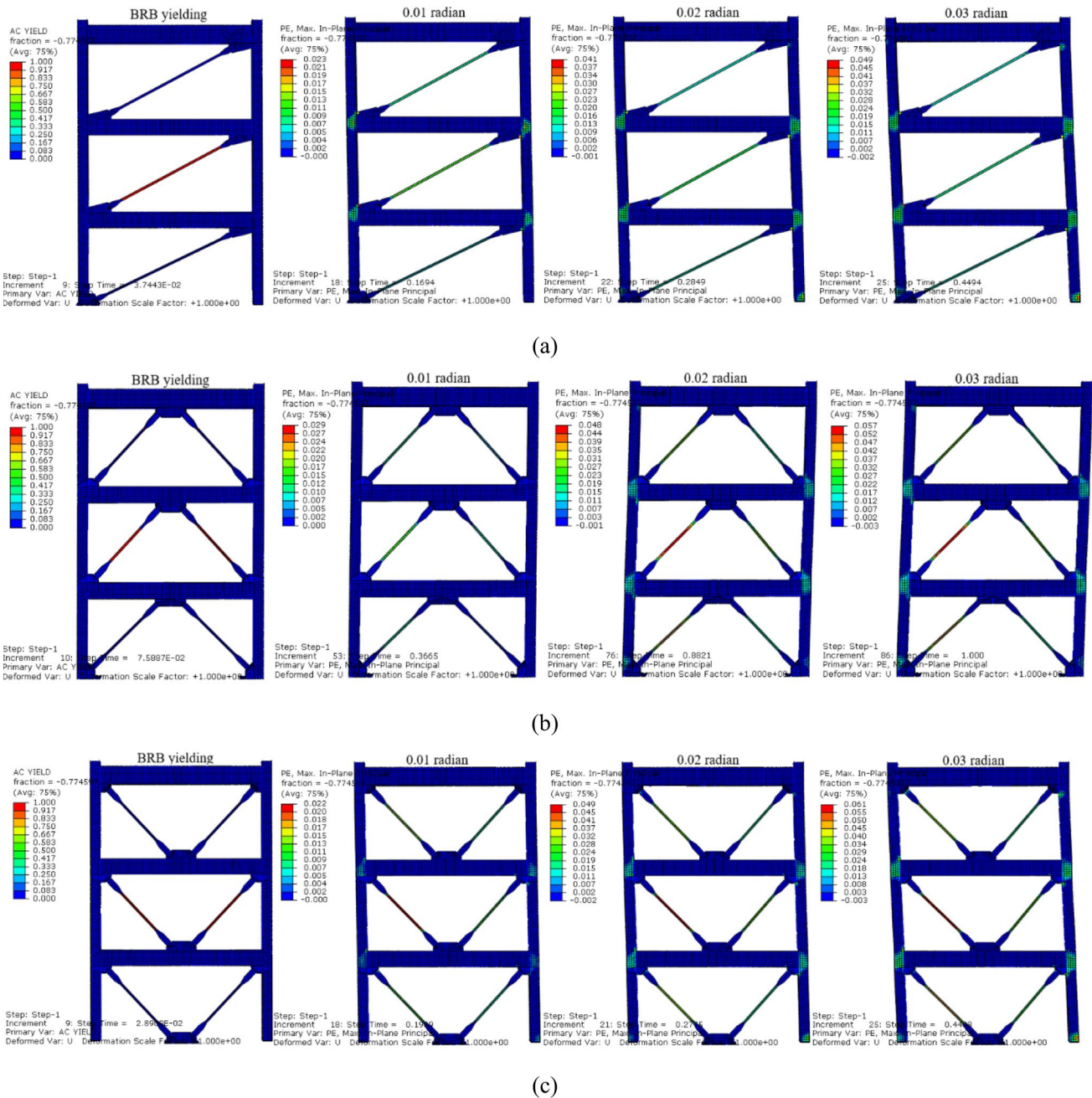


Fig. 17 Distribution of PE contours in different BRBF models: a Diagonal, b IV, c V. (PE: Plastic Strain)

sufficiently long descending branch with a 15% reduction, the ultimate displacement ( $\Delta_u$ ) is conservatively taken as the last recorded displacement. The yielding displacement signifies the transition from elastic to plastic behavior and is determined by the intersection of the idealized elastic and plastic branches of the load–displacement curve. The ductility factor ( $\mu$ ), calculated as the ratio of ultimate displacement to yielding displacement, quantifies a structure’s capacity to sustain deformations beyond the elastic limit.

### 6.2.3 Pushover Results

As illustrated in Figs. 19 and 20, a comparative pushover analysis was conducted to examine the roof displacement–base shear relationship for two- and three-story models with varying bracing configurations. The figures show that BRBF and HBRBF models exhibited comparable initial stiffness. However, due to the inclusion of the LYP160 core, HBRBFs initiated yielding at lower drift than BRBFs, which benefited from the higher yield strength of the SA440B core. This



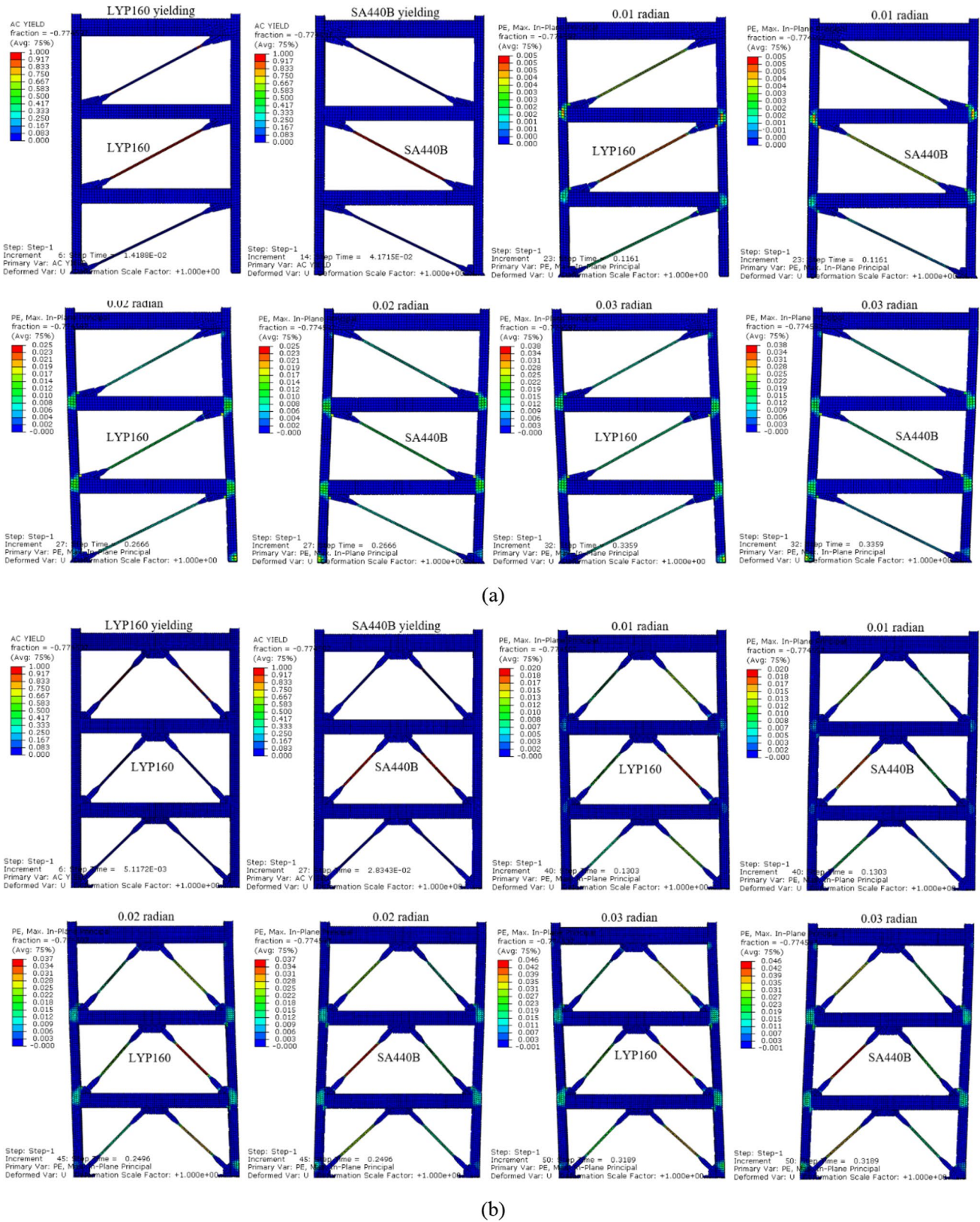


Fig. 18 Distribution of PE contours in different HBRBF models: a Diagonal, b IV, c V

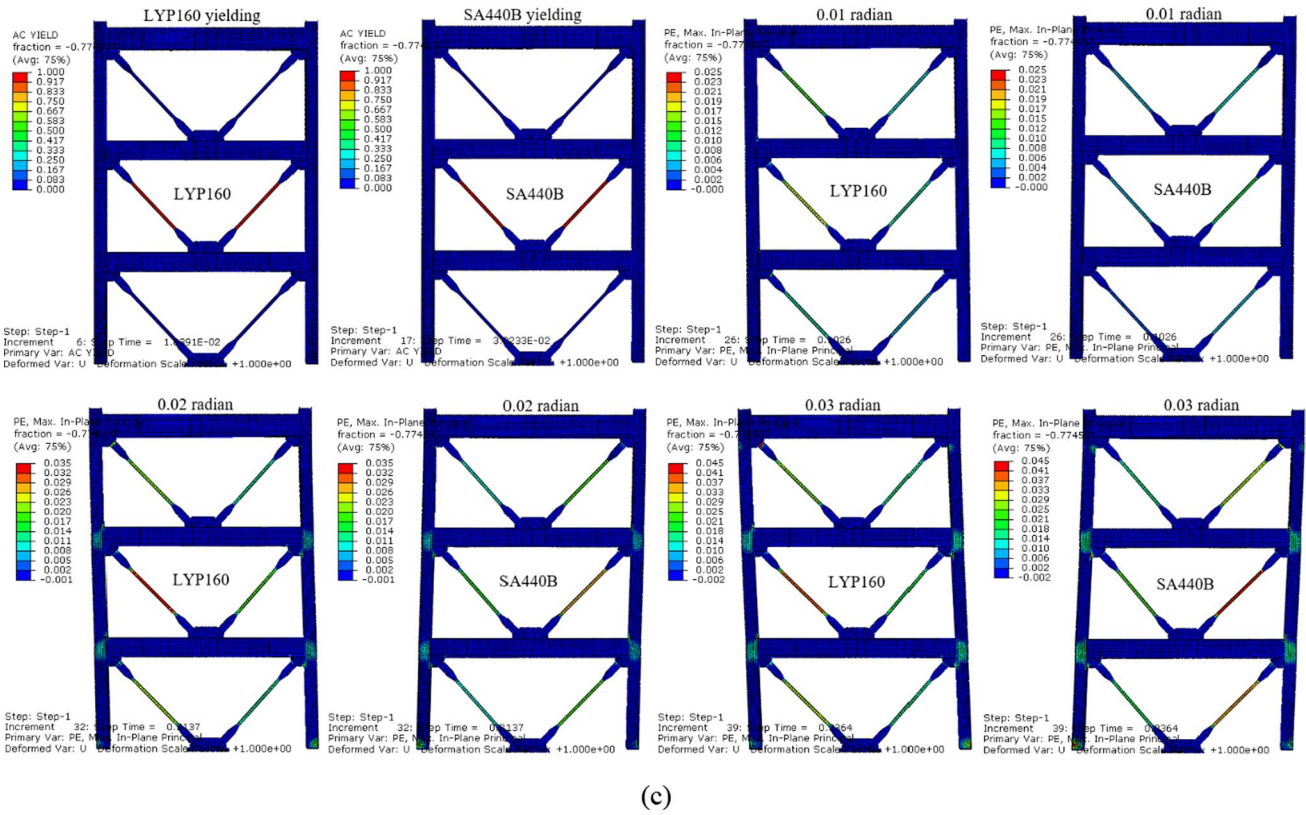


Fig. 18 (continued)

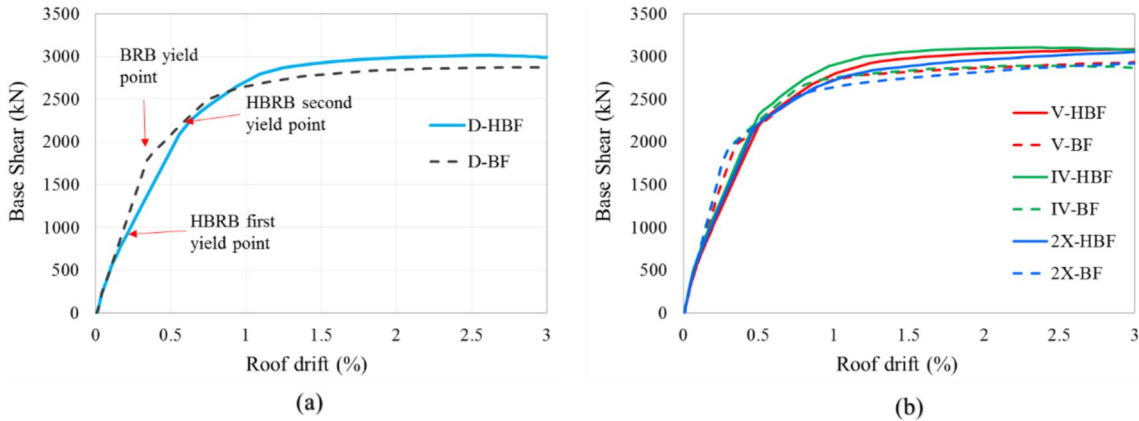


Fig. 19 Comparative pushover curve of two-story models

two-stage yielding behavior observed in HBRBFs translates to increased stiffness compared to BRBFs after the initial yielding point of the HBRBFs. Consequently, HBRBFs effectively mitigate the negative impact of P-Δ effects. This characteristic makes them particularly advantageous in medium- and high-rise buildings, where significant gravity loads contribute to substantial P-Δ effects.

Notably, the total brace strength was constant across BRBF and HBRBF models. The high strain hardening

property of the LYP160 core contributes to an enhancement in both the post-yield stiffness and the ultimate strength of the pushover curves for HBRBFs. As an examples of 2 and 3-story models, Figs. 19a and 20a depict the yield point for BRBFs and the primary and secondary yielding points for HBRBFs. While the elastic region of BRBFs is larger than that of HBRBFs due to the higher yield strength of the A572 core, their post-yield stiffness experiences a significant decrease.

Tables 4 and 5 present the behavioral parameters of the models derived from their bilinear response curves. The  $\Delta_s$  and  $\Delta_y$  columns reveal that, among the two-story models, the D-HBF exhibits the greatest displacements due to its longer HBRB core length compared to other bracing systems. This trend persists in the three-story frames, where D-HBF and Z-HBF experience larger displacements than V-HBF and IV-HBF. The tables show that BRBFs possess higher ductility than HBRBFs in two- and three-story frames. This observation can be attributed to the lower  $\Delta_y$  values exhibited by BRBFs in their idealized bilinear

capacity curves compared to HBRBFs. The maximum ductility for two-story models is observed in the 2X-BF model, reaching a value of 8.17. The V-BF model exhibits the highest ductility for three-story models, reaching 4.33. Within the HBRBF category, the 2X-BF and Inv. V models demonstrate the greatest ductility, attaining values of 6.2 and 3.95 in two- and three-story frames, respectively.

An analysis of the  $R_u$  parameter in Tables 4 and 5 reveals lower values for HBRBF models than their BRBFs. This disparity can be primarily attributed to the higher ductility of BRBFs, which significantly impacts the calculation of

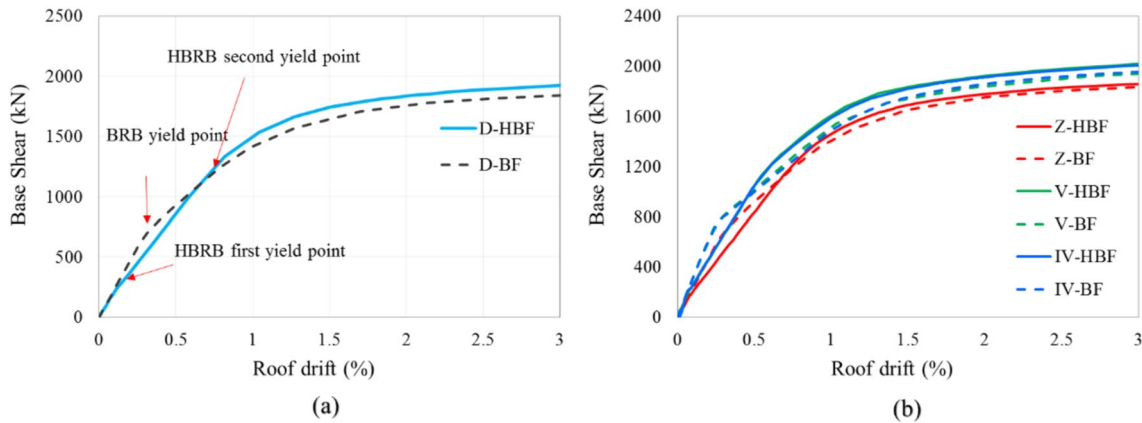


Fig. 20 Comparative pushover curve of three-story models

Table 4 Numerical results of two-story models

Model	$\Delta_s$	$\Delta_y$	$\Delta_u$	$V_s$	$V_y$	$V_u$	Ductility	$R_u$	$\Omega$	R
name	(mm)	(mm)	(mm)	(kN)	(kN)	(kN)	$\mu$			
D-HBF	17.2	52.1	240.0	957.0	3151.1	3064.3	4.61	2.87	3.29	9.44
D-BF	27.4	39.6	240.0	1322.9	2647.1	2947.5	6.05	3.33	2.31	7.70
V-HBF	16.4	43.2	240.0	1057.0	3140.7	3129.2	5.56	3.18	2.97	9.45
V-BF	30.1	34.9	240.0	1458.7	2656.0	3005.0	6.88	3.57	2.10	7.51
IV-HBF	16.3	41.1	240.0	1095.0	3261.2	3139.0	5.84	3.27	2.98	9.73
IV-BF	30.1	31.0	240.0	1450.8	2702.0	2955.0	7.74	3.81	2.15	8.19
2X-HBF	15.7	38.7	240.0	1063.0	3024.2	3111.0	6.20	3.38	2.84	9.61
2X-BF	29.2	29.4	240.0	1453.7	2544.0	2975.0	8.17	3.92	2.02	7.91

Table 5 Numerical results of three-story models

Model	$\Delta_s$	$\Delta_y$	$\Delta_u$	$V_s$	$V_y$	$V_u$	Ductility	$R_u$	$\Omega$	R
name	(mm)	(mm)	(mm)	(KN)	(KN)	(KN)	$\mu$			
D-HBF	20.4	90.9	290.5	414.8	1700.4	1969.3	3.20	2.32	3.69	8.57
D-BF	29.1	75.8	290.5	713.5	1570.6	1897.2	3.83	2.58	2.54	6.56
Z-HBF	19.7	91.0	290.5	398.4	1692.0	1940.0	3.19	2.32	3.82	8.87
Z-BF	27.6	78.1	290.5	672.3	1575.6	1883.1	3.72	2.54	2.71	6.87
V-HBF	17.2	75.4	290.5	426.8	1695.6	2025.3	3.85	2.59	3.58	9.26
V-BF	23.9	67.1	290.5	754.1	1579.9	1949.5	4.33	2.77	2.42	6.70
IV-HBF	16.4	73.5	290.5	421.8	1714.3	2068.3	3.95	2.63	3.66	9.61
IV-BF	23.9	72.4	290.5	748.6	1654.0	2013.0	4.01	2.65	2.55	6.76

$R_u$ . On average, two-story BRBF models exhibit a  $R_u$  value of 3.66, while HBRBF models possess a value of 3.17. This result translates to a 15% increase in  $R_u$  for BRBFs compared to HBRBFs. Similarly, BRBF  $R_u$  values demonstrate a 7% increase for three-story models relative to HBRBFs.

Furthermore, the coefficient of overstrength ( $\Omega$ ) for two-story BRBF models exhibits a range of 2.02 (2X-BF model) to 2.31 (D-BF model). Interestingly, HBRBF models exhibit a significantly higher average value of this parameter (41%), ranging from 2.84 to 3.29, compared to BRBFs. This discrepancy can be explained by the contrasting values of  $V_s$  and  $V_y$  parameters in HBRBF models compared to BRBFs, as detailed in the corresponding column of Table 4. Similarly, Table 5 demonstrates a 44% increase in the  $\Omega$  parameter for three-story hybrid models compared to their conventional brace model counterparts.

In conclusion, various models' response modification factor ( $R$ ) is evaluated. Table 4 demonstrates that  $R$  for hybrid models (D-HBF: 9.44 – IV-HBF: 9.73) surpasses that of conventional models (7.51–8.19). Analysis reveals a 22% increase in the average  $R$  of hybrid models (9.56) compared to conventional models (7.83). This enhancement primarily stems from hybrid models' elevated  $\Omega$  parameter values despite their lower average ductility than BRBFs. Similarly, for three-story models, the  $R$  values of D-HBF, Z-HBF, V-HBF, and IV-HBF are 8.57, 8.87, 9.26, and 9.61, respectively, averaging 9.08. This result represents a 35% increase compared to the corresponding BRBF models' average (6.72). Therefore, unlike BRBs, the proposed HBRB device exhibits significant potential in mitigating seismic collapse risks in steel-braced frames, establishing itself as a compelling alternative to conventional BRBs. Previous research by Asgarian and Shokrgozar (2009) suggested a seismic response modification factor of 8.35 for conventional BRBFs. Current code-compliant seismic designs, such as ASCE 7–22 (2022) and ANSI/AISC 341–22 (2022), prescribe a constant  $R$  factor of 7–8 for conventional BRBFs. Notably, this study reveals diverse  $R$  factors based on brace type. Consequently, ongoing research necessitates revising and updating BRB provisions within seismic standards to facilitate safer and more economical structural design.

### 6.3 Earthquake Responses

Seven ground motion records were used to evaluate the seismic behavior of structural models equipped with BRBs and HBRBs. These records were selected based on different magnitude characteristics, distance from the fault, type of fault, and peak ground acceleration. Table 6 details these ground motion records. These ground motions are used for nonlinear incremental dynamic and time history analysis.

#### 6.3.1 Incremental Dynamic Analysis

Incremental dynamic analysis (IDA) involves a series of nonlinear dynamic analyses conducted under a suite of earthquake ground motions. In this analysis, the target structure is subjected to dynamic excitations from various seismic events, and the maximum structural response is subsequently captured. For this study, the maximum inter-story drift was chosen as the damage metric, a parameter deemed to exceed 2.5% (3%) for braced frames, as per ANSI/AISC341-22 (2022). The spectral acceleration ( $S_a$ ) of the first mode was selected as the intensity measure parameter. In accordance with ASCE7-22 (2022), seven ground motion records were employed in the IDA analysis. As an illustrative example, Fig. 21 presents the IDA curves for 3-story diagonal and inverted braced frames, including both BRBF and HBRBF configurations. As depicted in Fig. 21, HBRBFs demonstrate a higher capacity to withstand higher  $S_a$  values compared to BRBFs.

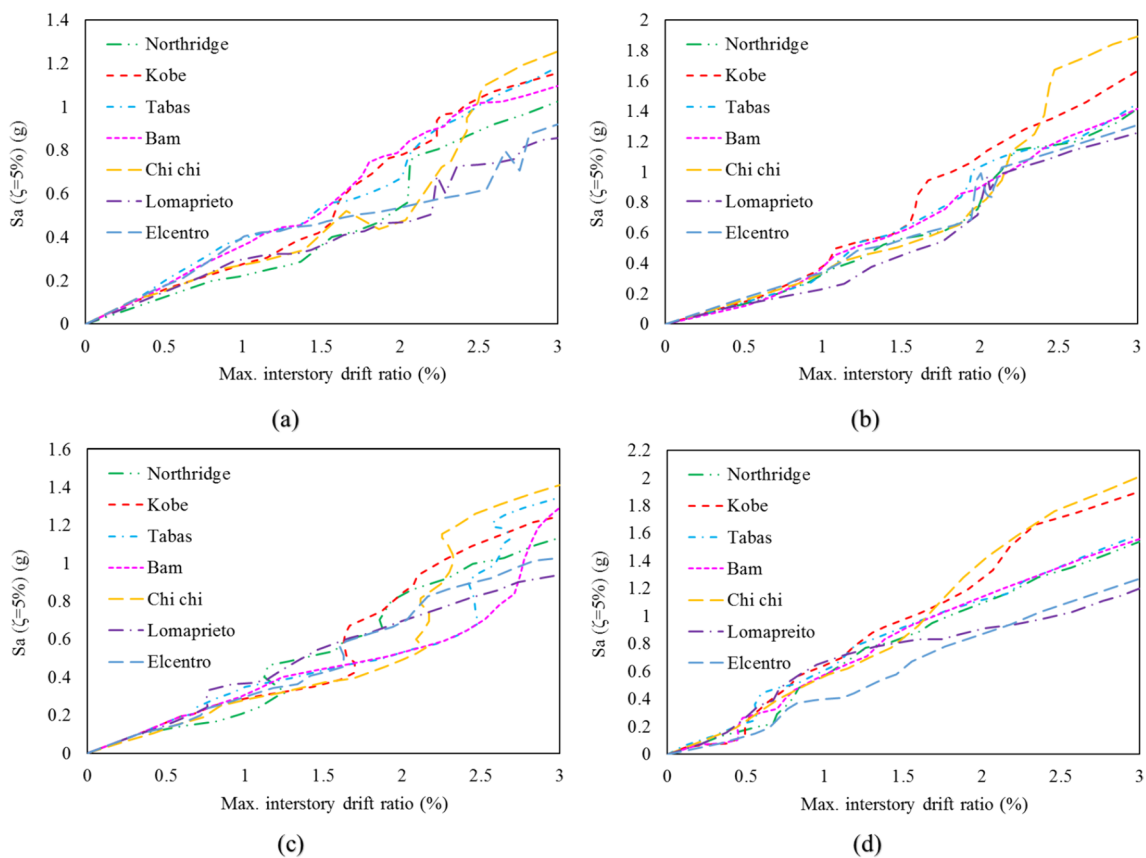
After performing IDA, the resulting dynamic pushover curves of the studied frames were extracted and presented in this section. For instance, incremental dynamic analysis results were compared to the static pushover curve regarding the roof displacement-base shear relationship for 3-story diagonal and Inverted-V braced frames, as illustrated in Figs. 22a to d.

Figure 22 illustrates a reduction in stiffness and strength exhibited by the dynamic pushover curves of BRBFs post-yield. Conversely, the dynamic pushover curves of HBRBFs demonstrate negligible strength loss and predominantly positive post-yield stiffness. After conducting IDA analysis and employing the pushover curve depicted in Fig. 22, response modification factor values were computed for each model and tabulated in Table 7. As indicated in this Table, a distinct response modification factor value is observed for each record. Additionally, average response modification factor parameters were determined and included in the Table's conclusion.

Seismic performance parameters and response modification factors were computed for all examined frames to facilitate model comparison and overall analysis interpretation.

**Table 6** Ground motion data

No	Earth. name	Year	Station	Mag	PGA
1	Northridge	1994	Canyon	6.7	0.48
2	Kobe, Japan	1995	Nishi- Akashi	6.9	0.51
3	Tabas	1978	Tabas	7.4	0.92
4	Bam	2003	Abaragh	6.6	0.17
5	Chi-Chi	1999	TCU084	7.6	1.01
6	Loma Prieta	1989	Capitola	6.9	0.53
7	Elcentro	1940	El Centro Array #9	6.9	0.32



**Fig. 21** IDA curves for the 3-story models, **a** D-BF, **b** D-HBF, **c** IV-BF, and **d** IV-HBF

The corresponding values, including the response modification factor ( $R$ ), are tabulated in Table 8. A review of this Table reveals that HBRB models consistently exhibit higher response modification factors than BRB models across two- and three-story configurations with varying bracing arrangements. Two-story structures equipped with HBRBFs demonstrated an average response modification factor of 12.73, surpassing BRBFs by 39.4%. Similarly, a 59.6% increase in the average  $R$ -value was observed for three-story HBRBF models compared to their BRBF counterparts, with respective values of 11.56 and 7.24.

As indicated by Table 8, the mean values of  $\Omega$  and  $R_{\mu}$  for two- and three-story HBRBFs are calculated to be 4.89 and 2.51, respectively. These values represent increases of 87% and decrease of 20% relative to their BRBF counterparts, which are 2.6 and 3.17. Upon analysis of the frames investigated in this study, a substantial performance enhancement of HBRBFs is observed, with an average  $R$ -value increase of 50% compared to the corresponding BRBF structures.

Table 9 provides a comparative analysis of response modification factor parameters for pushover and dynamic analysis methodologies. Tabulated data reveals that, except for the  $R_{\mu}$  coefficient in HBRBFs, the parameter values associated

with dynamic analysis consistently exceed those obtained from pushover analysis.

### 6.3.2 Time History Analysis

Three ground motion histories were selected from a pool of seven records to facilitate the computation of maximum inter-story drift ratio (IDR) and residual inter-story drift ratio (RIDR) for braced frames. In order to obtain the roof drift ratio and free vibration simulation at the end of the analysis, after performing the analysis, the assumption of zero acceleration for 20 s was applied.

For 2-story diagonal braced frames, as depicted in Fig. 23, the time history of roof drift reveals pronounced nonlinear behavior in both frames, with comparable peak demands. Nevertheless, a more minor residual deformation is observed in the HBRBF. This phenomenon is elucidated through an examination of the time history responses. The most intense seismic pulse induces roof drift ratios of 1.05% and 1.28% in the HBRBF and BRBF, respectively, for the two-story frames. Subsequent reversal pulses instigate oscillatory motion in the opposite direction, leading to a recovery of the deformed configurations toward their initial positions.

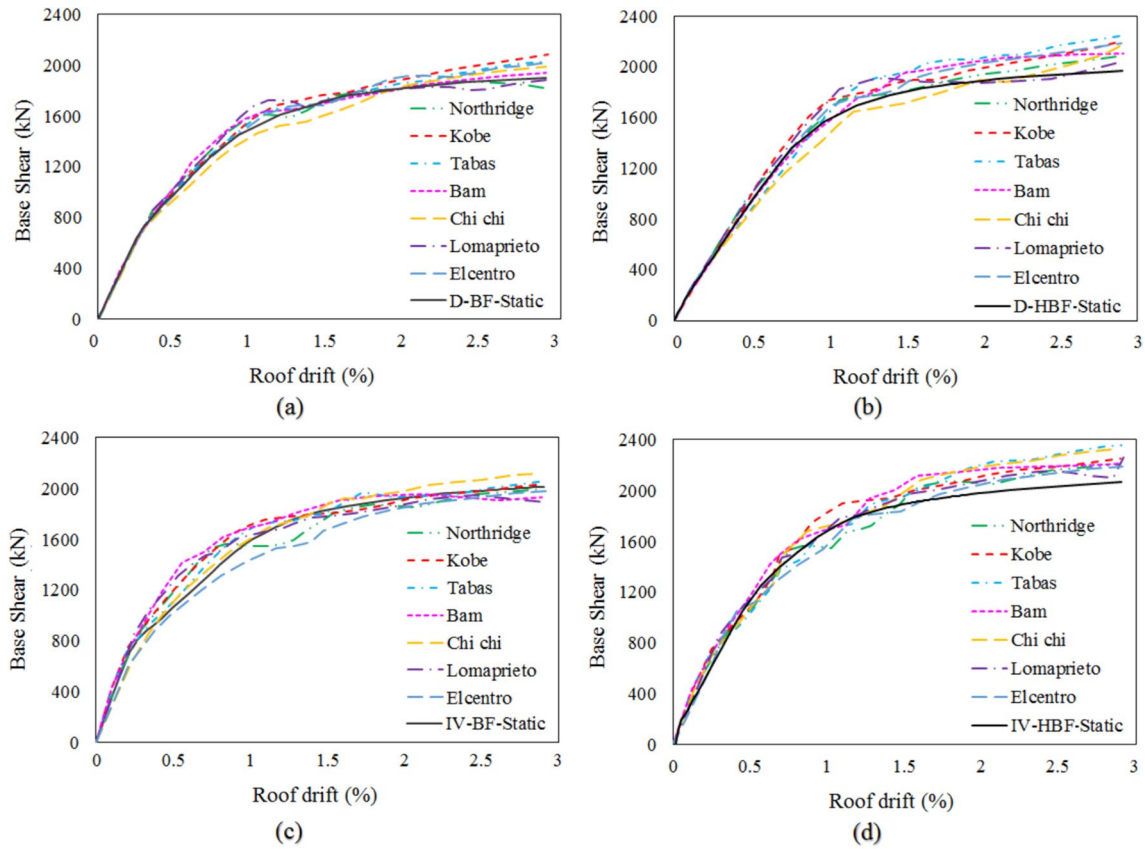


Fig. 22 Incremental dynamic roof displacement–the base shear curve of 3-story models, **a** D-BF, **b** D-HBF, **c** IV-BF, and **d** IV-HBF

Table 7 Response modification factor of the diagonal and IV brace models

Records	Model	Diagonal						IV					
		$V_b$ (Dyn, u) (kN)	$V_b$ (St, y) (kN)	$V_b$ (Dyn, e) (kN)	$\Omega$	$R_\mu$	R	$V_b$ (Dyn, u) (kN)	$V_b$ (St, y) (kN)	$V_b$ (Dyn, e) (kN)	$\Omega$	$R_\mu$	R
Elcentro	HBF	2182.6	414.8	4605.4	5.26	2.11	11.10	2191.0	426.8	4929.8	5.13	2.25	11.55
	BF	2021.1	713.5	5254.7	2.83	2.60	7.36	1979.3	754.1	5344.0	2.62	2.70	7.09
Kobe	HBF	2199.2	414.8	4706.2	5.30	2.14	11.35	2256.2	426.8	5189.3	5.29	2.30	12.16
	BF	2083.8	713.5	5647.1	2.92	2.71	7.91	2038.1	754.1	5727.1	2.70	2.81	7.59
Tabas	HBF	2240.5	414.8	4951.5	5.40	2.21	11.94	2358.0	426.8	5682.8	5.52	2.41	13.31
	BF	2032.2	713.5	5202.4	2.85	2.56	7.29	2061.5	754.1	5524.8	2.73	2.68	7.33
Bam	HBF	2108.2	414.8	4385.1	5.08	2.08	10.57	2212.0	426.8	5043.2	5.18	2.28	11.82
	BF	1936.8	713.5	5306.9	2.71	2.74	7.44	1935.0	754.1	5398.7	2.57	2.79	7.16
Chi chi	HBF	2166.1	414.8	4592.1	5.22	2.12	11.07	2323.0	426.8	5505.5	5.44	2.37	12.90
	BF	1989.5	713.5	5152.7	2.79	2.59	7.22	2119.5	754.1	5743.7	2.81	2.71	7.62
Northridge	HBF	2091.7	414.8	4288.0	5.04	2.05	10.34	2207.3	426.8	5032.7	5.17	2.28	11.79
	BF	1821.1	713.5	5062.5	2.55	2.78	7.10	1994.0	754.1	5643.0	2.64	2.83	7.48
Lomapreito	HBF	2042.1	414.8	4043.3	4.92	1.98	9.75	2260.8	426.8	4996.3	5.30	2.21	11.71
	BF	1887.8	713.5	4285.3	2.65	2.27	6.01	1891.0	754.1	4519.4	2.51	2.39	5.99
Average	HBF	2147.2	414.8	4510.2	5.18	2.10	10.87	2258.3	426.8	5197.1	5.29	2.30	12.18
	BF	1967.5	713.5	5130.2	2.76	2.61	7.19	2002.6	754.1	5414.4	2.66	2.70	7.18

**Table 8** Response modification factor of the models

Model	2-Story						3-Story						
	$V_b$ (Dyn, u) (kN)	$V_b$ (St, y) (kN)	$V_b$ (Dyn, e) (kN)	$\Omega$	$R_\mu$	R	Model	$V_b$ (Dyn, u) (kN)	$V_b$ (St, y) (kN)	$V_b$ (Dyn, e) (kN)	$\Omega$	$R_\mu$	R
D-HBF	4560.0	957.0	11,491.2	4.76	2.52	12.01	D-HBF	2147.2	414.8	4510.2	5.18	2.10	10.87
D-BF	3448.6	1322.9	11,587.2	2.61	3.36	8.76	D-BF	1967.5	713.5	5130.2	2.76	2.61	7.19
V-HBF	4731.4	1057.0	13,484.3	4.48	2.85	12.76	Z-HBF	2153.3	398.4	4414.3	5.40	2.05	11.08
V-BF	3576.0	1458.7	12,837.7	2.45	3.59	8.80	Z-BF	1953.9	672.3	5021.4	2.91	2.57	7.47
IV-HBF	4783.8	1095.0	14,160.2	4.37	2.96	12.93	V-HBF	2216.7	426.8	5164.8	5.19	2.33	12.10
IV-BF	3486.9	1450.8	13,459.4	2.40	3.86	9.28	V-BF	1949.4	754.1	5380.3	2.59	2.76	7.13
2X-HBF	4703.8	1063.0	14,064.5	4.43	2.99	13.23	IV-HBF	2258.3	426.8	5197.1	5.29	2.30	12.18
2X-BF	3570.0	1453.7	14,101.5	2.46	3.95	9.70	IV-BF	2002.6	754.1	5414.4	2.66	2.70	7.18

**Table 9** Response modification factors from incremental dynamic and pushover analysis

Frames	Parameters	BRBF		HBRBF	
		Pushover analysis	Incremental dynamic analysis	Pushover analysis	Incremental dynamic analysis
2-story	$\Omega$	2.15	2.48	3.02	4.51
	$R_\mu$	3.66	3.69	3.17	2.83
	R	7.83	9.13	9.56	12.73
3-story	$\Omega$	2.56	2.73	3.69	5.27
	$R_\mu$	2.63	2.66	2.46	2.19
	R	6.72	7.24	9.08	11.56

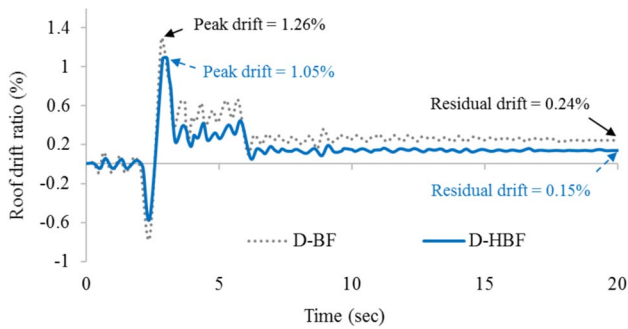


**Fig. 23** Time history response of roof drift ratio for 2-story diagonal braced frames

Ultimately, the BRBF exhibits a residual roof drift of 0.24%, contrasting with the 0.15% value recorded for the HBRBF. This discrepancy is attributed to the staged yielding and positive post-yield stiffness characteristics of the HBRB.

The maximum IDR and RIDR were calculated using time history analysis for all models. Figure 24 visualizes the resultant data for BRB core and HBRB core configurations. Figures 24a and c present the IDR values for braced frames subjected to three ground motions. The IDR of HBRBFs is lower than that of BRBFs, suggesting that the proposed

HBRB system is relatively effective in mitigating maximum deformations induced by seismic events. For two-story models, average residual drift ratios of 0.66% and 0.81% are calculated for HBRBFs and BRBFs, respectively. These values increase to 0.88% and 1.09% for the corresponding three-story models. On average, a 17% reduction in IDR is observed for two-story HBRBFs compared to BRBFs, increasing to a 19% reduction for three-story frames.

In contrast, Fig. 24b and d reveal more pronounced reductions in RIDR values than IDR. For two-story models, average RIDR values of 0.09% and 0.14% are determined for HBRBFs and BRBFs, respectively, indicating a 39% decrease in RIDR for HBRBFs. A similar trend is evident in the three-story models, where a 46% average reduction in RIDR is calculated for HBRBFs relative to BRBFs.

Thus, it can be concluded that HBRBs are suitably efficient in mitigating residual displacements within bracing frames. This finding aligns with Jia et al.'s investigations (2018). Furthermore, owing to the P-delta effect in high-rise structures and those exhibiting higher vibration periods, the proposed bracing system is anticipated to demonstrate enhanced efficacy within such structures, as cited by Heshmati et al. (2022).

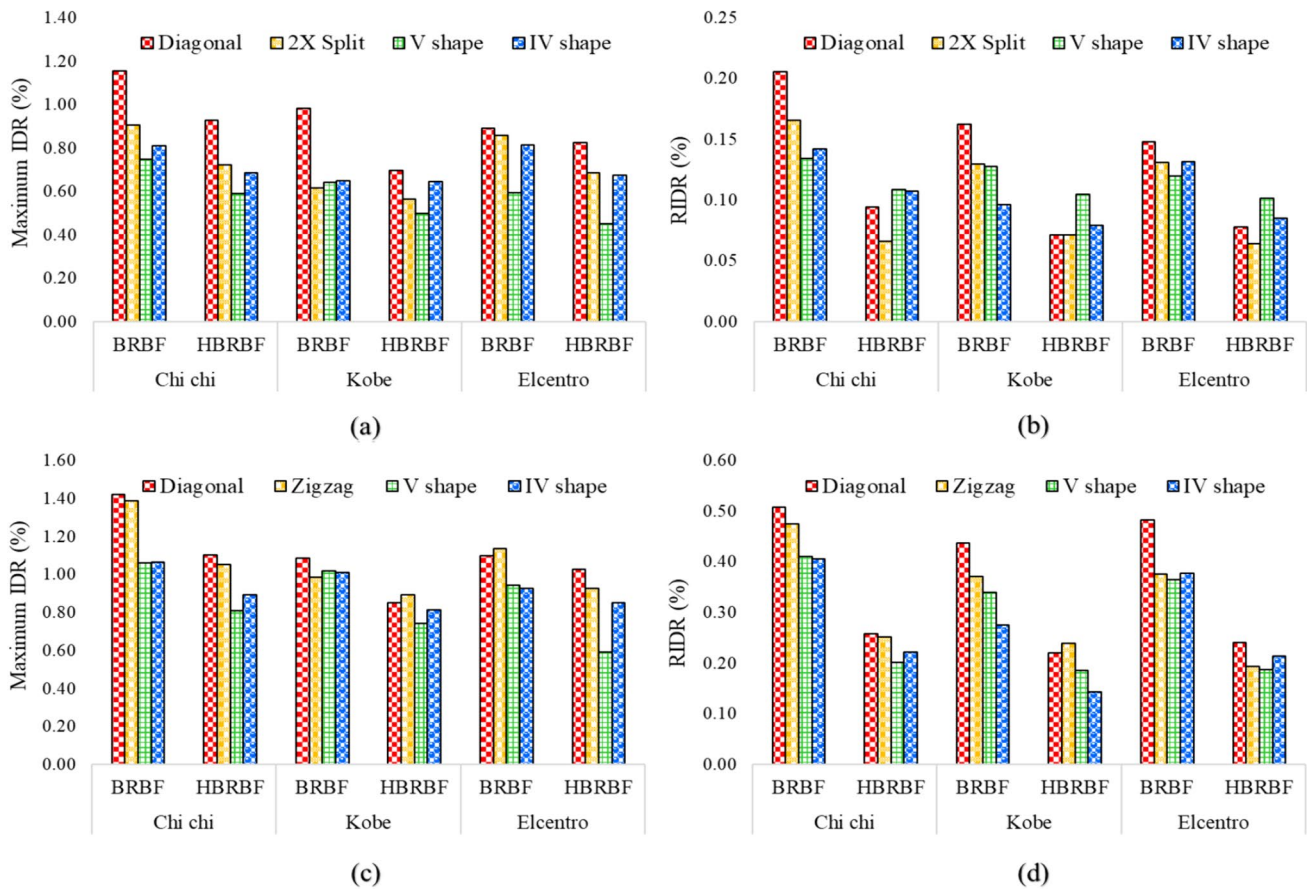


Fig. 24 The maximum IDR and RIDR for braced frames: **a, b** 2- story; **c, d** 3- story

## 7 Conclusion

This study investigated the application of hybrid buckling-restrained braces (HBRBs) as a potential solution to the inherent weakness of conventional BRBs, namely their low post-yield stiffness. HBRBs, constructed with a composite of high-strength (SA440B) and low-yield point (LYP160) steels, were compared to traditional A572 steel core BRBs. Utilizing Abaqus software and a core-spring finite element model, we evaluated the cyclic response and potential seismic performance improvement of HBRBs in low-rise frames with various bracing configurations. Pushover and incremental dynamic analysis determined key seismic parameters for eight two-story and eight three-story models. Furthermore, time history analyses were conducted on the specified models to assess the efficacy of HBRBs in mitigating residual displacement. The major outcomes of this study are summarised as follows:

- Compared to bilinear kinematic hysteresis behavior observed in BRBs, HBRBs exhibit a trilinear kinematic hysteresis response with enhanced hardening characteristics. This point translates to fewer plastic displacements

experienced by HBRBs compared to their BRB counterparts.

- Due to the low yield point of the LYP160 core, HBRBF models employing this material exhibited earlier inelastic deformation compared to models utilizing BRBs. This early yielding, observed at both the member and frame level, signifies the initiation of energy dissipation mechanisms within the LYP160 cores. Conversely, the SA440B core, characterized by significantly higher yield strength, demonstrated delayed plastic behavior, with significant deformation occurring only at more considerable displacement demands.
- Pushover analysis revealed that the HBRB's LYP160 core exhibited substantial plastic deformation, thereby inhibiting or postponing the onset of plasticity within the frame elements.
- Two-story HBRBFs exhibited a 41% increase in over-strength coefficient ( $\Omega$ ) compared to BRBFs. This trend persisted in three-story models, where HBRBFs demonstrated a 44% higher coefficient. This disparity is primarily attributed to the lower  $V_s$  values observed in HBRBFs, which is a direct consequence of the ear-



lier yielding behavior of LYP160 steel compared to the steel employed in BRBFs.

- Pushover analysis revealed that the response modification factor ( $R$ ) in two-story HBRBFs exhibits a compelling range of 9.44 (D-HBF) to 9.73 (IV-HBF), surpassing the 7.51–8.19 range observed in conventional models. This result translates to a 22% increase in the average  $R$ -value for HBRBFs (9.56) compared to their conventional BRBFs counterparts (7.83). Notably, the three-story models exhibited a similar trend, with an average  $R$  of 9.08 for HBRBFs and 6.72 for conventional BRBFs, signifying a pronounced 35% enhancement in the  $R$  parameter for HBRBFs. This substantial improvement in  $R$  for HBRBFs can be primarily attributed to the elevated values of the  $\Omega$  parameter observed in these models.
- Incremental dynamic analysis revealed an enhancement in the  $R$ -value for HBRBFs compared to BRBFs. Specifically, a mean  $R$ -value of 12.73 was computed for two-story HBRBF structures, representing a 39.4% increase over the corresponding value of 9.13 for BRBFs. This trend persisted in three-story frames, with mean  $R$ -values of 11.56 and 7.24 observed for HBRBFs and BRBFs, respectively, indicating a 59.6% improvement. Furthermore, the average  $\Omega$  and  $R_u$  values for two- and three-story HBRBF configurations were determined to be 4.89 and 2.51, signifying augmentations of 87% and reductions of 20%, respectively, relative to BRBF counterparts with values of 2.6 and 3.17.
- A comparative analysis of pushover and incremental dynamic analysis outcomes for HBRB models indicated that the average overstrength and response modification factors derived from pushover analysis (3.4 and 9.3, respectively) were inferior to those determined through incremental dynamic analysis (4.9 and 12.1, respectively). Conversely, the ductility reduction factor calculated via pushover analysis (2.8) marginally exceeded its counterpart obtained from incremental dynamic analysis (2.5).
- Nonlinear time history analysis demonstrated that integrating HBRBs within the investigated models resulted in an average 18% reduction in IDR and 43% reduction in RIDR compared to those equipped with BRBs. Furthermore, the efficacy of HBRBs in mitigating RIDR was observed to be more pronounced in 3-story models relative to their 2-story counterparts.
- A comprehensive analysis of all seismic parameters indicates that model IV-HBF demonstrates better earthquake resistance than the other two- and three-story models. This exceptional performance can be attributed to its remarkable ductility and capacity to modify the seismic response.

As demonstrated, the results presented here provide a quantitative framework for evaluating the positive impact of HBRBs on structural response, which can aid in advancing current seismic design approaches. Nevertheless, the generalizability of these results necessitates further investigation by examining a broader spectrum of structural periods, alternative combinations of LYP and HSS materials, and a more expansive ground motion dataset. A comprehensive evaluation of the performance characteristics of this ductile lateral resistance system constitutes a probable avenue for future research endeavors.

**Author Contribution** H. A: Conceptualization, Methodology, Investigation, Software, Validation, Resources, Writing-Original Draft, Review & Editing. J. A: Supervision, Investigation, Methodology, Review & Editing, Validation, Writing-Original Draft.

**Data Availability** No datasets were generated or analysed during the current study.

## Declarations

**Conflict of interest** The authors declare no competing interests.

## References

- Abou-Elfath H (2017) Evaluating the ductility characteristics of self-centering buckling-restrained shape memory alloy braces. *Smart Mater Struct* 26(5):055020
- ANSI/AISC 341-22, 2022, Seismic provisions for structural steel buildings, American Institute of Steel Construction, Chicago, IL
- ASCE/SEI 7-22, 2022, Minimum design loads and associated criteria for buildings and other structures, American Society of Civil Engineering, Reston, VA
- Asgarian B, Shokrgozar HR (2009) BRBF response modification factor. *J Constr Steel Res* 65(2):290–298
- Atlayan O, Charney FA (2014) Hybrid buckling-restrained braced frames. *J Constr Steel Res* 96:95–105
- Azizi H, Ahmadi J (2024) Investigating the seismic behavior of low-rise steel frames equipped with dual-core self-centering buckling-restrained brace. *Soil Dyn Earthq Eng* 185:108905
- Azizi H, Ahmadi J, Eghbali M (2023) Study on self-centering mechanism of different yield strength hybrid buckling restrained braces. *J Constr Steel Res* 210:108068
- Bai J, Chen H, Ma G, Duan L (2022) Development of a four-tube-assembled buckling-restrained brace for convenient post-earthquake damage examination and replacement. *J Build Eng* 50:104209
- Ban H, Shi G (2018) A review of research on high-strength steel structures. *Proceed Inst Civil Eng-Struct and Build* 171(8):625–641
- Ban H, Shi G, Shi Y, Wang Y (2012) Overall buckling behavior of 460 MPa high strength steel columns: Experimental investigation and design method. *J Constr Steel Res* 74:140–150
- Barbagallo F, Bosco M, Marino EM, Rossi PP (2019) Achieving a more effective concentric braced frame by the double-stage yield BRB. *Eng Struct* 186:484–497
- Bjorhovde R (2004) Development and use of high-performance steel. *J Constr Steel Res* 60(3–5):393–400
- Bjorhovde R (2010) Performance and design issues for high strength steel in structures. *Adv Struct Eng* 13(3):403–411

- Budaházy V, Dunai L (2015) Numerical analysis of concrete filled buckling restrained braces. *J Constr Steel Res* 115:92–105
- Chen CC, Chen SY, Liaw JJ (2001) Application of low yield strength steel on controlled plastification ductile concentrically braced frames. *Can J Civil Eng* 28(5):823–836
- Chen L, Wang D, Shi F, Zhang R, Sun Z (2023) Hysteretic performance of self-centering buckling-restrained braces with embedded friction spring. *Eng Struct* 280(115595):6
- Das PJ, Deb SK (2022) Seismic performance evaluation of a new hybrid buckling restrained brace under cyclic loading. *J Struct Eng* 148(6):04022069
- Fukumoto Y (1996) New construction steels and structural stability. *Eng Struct* 18(10):786–791
- Heshmati M, Tameh M, Khatami A (2022 May). Seismic-resilient diagrid structures with hybrid buckling restrained braces. In *Structures* 39:218–236
- Hoveidae N, Radpour S (2021) A novel all-steel buckling restrained brace for seismic drift mitigation of steel frames. *Bull Earthq Eng* 19:1537–1567
- Hu F, Shi G, Shi Y (2017) Experimental study on seismic behavior of high strength steel frames: global response. *Eng Struct* 131:163–179
- Hu F, Shi G, Shi Y (2018) Constitutive model for full-range elastoplastic behavior of structural steels with yield plateau: formulation and implementation. *Eng Struct* 171:1059–1070
- Hu B, Min Y, Wang C, Xu Q, Keleta Y (2022) Design, analysis and application of the double-stage yield buckling restrained brace. *J Build Eng* 48:103980
- Jia M, Lu D, Guo L, Sun L (2014) Experimental research and cyclic behavior of buckling-restrained braced composite frame. *J Constr Steel Res* 95:90–105
- Jia LJ, Li RW, Xiang P, Zhou DY, Dong Y (2018) Resilient steel frames installed with self-centering dual-steel buckling-restrained brace. *J Constr Steel Res* 149:95–104
- Jiang ZQ, Dou C, Guo YL, Zhang AL (2017) Theoretical study on design methods for pinned assembled BRB with flat core. *Eng Struct* 133:1–13
- Kachooee A, Kafi MA (2018) A suggested method for improving post buckling behavior of concentric braces based on experimental and numerical studies. In *Structures* 14:333–347
- Khoo HH, Tsai KC, Tsai CY, Tsai CY, Wang KJ (2016) Bidirectional substructure pseudo-dynamic tests and analysis of a full-scale two-story buckling-restrained braced frame. *Earthq Eng Struct Dynam* 45(7):1085–1107
- Kim DH, Lee CH, Ju YK, Kim SD (2015) Subassemblage test of buckling-restrained braces with H-shaped steel core. *Struct Design Tall Spec Build* 24(4):243–256
- Lam SSE, Wu B, Wong YL, Wang ZY, Liu ZQ, Li CS (2003) Drift capacity of rectangular reinforced concrete columns with low lateral confinement and high-axial load. *J Struct Eng* 129(6):733–742
- Lin PC, Tsai KC, Wang KJ, Yu YJ, Wei CY, Wu AC, Roeder CW (2012) Seismic design and hybrid tests of a full-scale three-story buckling-restrained braced frame using welded end connections and thin profile. *Earthq Eng Struct Dyn* 41(5):1001–1020
- Mwafy AM, Elnashai AS (2002) Calibration of force reduction factors of RC buildings. *J Earthq Eng* 6(02):239–273
- Naghavi M, Rahnavard R, Thomas RJ, Malekinejad M (2019) Numerical evaluation of the hysteretic behavior of concentrically braced frames and buckling restrained brace frame systems. *J Build Eng* 22:415–428
- Nakashima M, Roeder CW, Maruoka Y (2000) Steel moment frames for earthquakes in United States and Japan. *J Struct Eng* 126(8):861–868
- Newmark, NM, Hall WJ (1982). *Earthquake spectra and design. Engineering monographs on earthquake criteria*
- Pan P, Li W, Nie X, Deng K, Sun J (2017) Seismic performance of a reinforced concrete frame equipped with a double-stage yield buckling restrained brace. *Struct Design Tall Spec Build* 26(4):e1335
- Qu B, Liu X, Hou H, Qiu C, Hu D (2018) Testing of buckling-restrained braces with replaceable steel angle fuses. *J Struct Eng* 144(3):04018001
- Rahnavard R, Naghavi M, Aboudi M, Suleiman M (2018) Investigating modeling approaches of buckling-restrained braces under cyclic loads. *Case Stud in Constr Mater* 8:476–488
- Raoul, J. (2005). *Use and application of high-performance steels for steel structures (Vol. 8)*. Iabse
- SAC 2000, *Steel moment frame connection advisory no. 3*, prepared by the SAC joint venture for the federal emergency management agency. Washington, DC
- SEAOC structural/seismic design manual, 2021 IBC, Volume 4, Examples for steel-framed buildings, 8, International Code Council, Structural Engineering Association of California
- Shen J, Seker O, Akbas B, Seker P, Momenzadeh S, Faytarouni M (2017) Seismic performance of concentrically braced frames with and without brace buckling. *Eng Struct* 141:461–481
- Shi G, Gao Y, Wang X, Zhang Y (2018a) Mechanical properties and constitutive models of low yield point steels. *Constr Build Mater* 175:570–587
- Shi G, Yin H, Hu F (2018b) Experimental study on seismic behavior of full-scale fully prefabricated steel frame: global response and composite action. *Eng Struct* 169:256–275
- Shi G, Gao Y, Wang X (2019) Material properties and partial factors for resistance of low yield point steels in China. *Constr Build Mater* 209:295–305
- Shi G, Zhao H, Gao Y (2022) Development of triple grades hybrid high-performance steel structure (TGHSS): concept and experiments. *Eng Struct* 266:114654
- Shi Y, Zhang Z, Fan X, Han J, Qin H, Sun Z (2023) Seismic design and performance analysis of bridge bents retrofitted with multistage buckling-restrained braces. In *Structures* 49:779–791
- Sitler B, Takeuchi T (2020) Reducing residual drift with multistage buckling-restrained braces. *J Constr Steel Res* 159:260–269
- Sitler B, Takeuchi T, Matsui R, Terashima M, Terazawa Y (2020) Experimental investigation of a multistage buckling-restrained brace. *Eng Struct* 213:110482
- Sitler B, Takeuchi T (2019) Effect of steel grade and core yield length in multistage buckling-restrained braces subjected to mainshock-aftershock sequences. In *Pacific Struct Steel Conf*
- Sugisawa M, Saeki E, Nakamura H, Hirabayashi R, Ichikawa Y, Ueki M, Hokari M (1995) Development of earthquake-resistant, vibration control, and base isolation technology for building structures. Nippon Steel Technical Report 66:37–46
- Sun J, Pan P, Wang H (2018) Development and experimental validation of an assembled steel double-stage yield buckling restrained brace. *J Constr Steel Res* 145:330–340
- Tenchini A, D'Aniello M, Rebelo C, Landolfo R, da Silva LS, Lima L (2016) High strength steel in chevron concentrically braced frames designed according to Eurocode 8. *Eng Struct* 124:167–185
- Tong JZ, Guo YL (2017) Global buckling prevention of end collared buckling-restrained braces: theoretical, numerical analyses and design recommendations. *Eng Struct* 152:289–306
- Tong JZ, Guo YL (2018) Numerical investigations on elastic buckling and hysteretic behavior of steel angles assembled buckling-restrained braces. *J Constr Steel Res* 144:21–39
- Uang CM (1991) Establishing R (or R<sub>w</sub>) and C<sub>d</sub> factors for building seismic provisions. *J Struct Eng* 117(1):19–28
- Wang T, Hsu TT (2001) Nonlinear finite element analysis of concrete structures using new constitutive models. *Comput Struct* 79(32):2781–2791

- Wang J, Shi Y, Wang Y (2016) Constitutive model of low-yield points steel and its application in numerical simulation of buckling-restrained braces. *J Mater Civ Eng* 28(3):04015142
- Wang CL, Chen Q, Zeng B, Meng S (2017a) A novel brace with partial buckling restraint: an experimental and numerical investigation. *Eng Struct* 150:190–202
- Wang M, Fahnestock LA, Qian F, Yang W (2017b) Experimental cyclic behavior and constitutive modeling of low yield point steels. *Constr Build Mater* 131:696–712
- Wu B, Mei Y (2015) Buckling mechanism of steel core of buckling-restrained braces. *J Constr Steel Res* 107:61–69
- Yakhchalian M, Asgarkhani N, Yakhchalian M (2020) Evaluation of deflection amplification factor for steel buckling restrained braced frames. *J Build Eng* 30:101228
- Yang L, Gao Y, Shi G, Wang X, Bai Y (2018) Low cycle fatigue property and fracture behavior of low yield point steels. *Constr Build Mater* 165:688–696
- Yang C, Xie L, An N, Li A, Liu Q, Wang X (2023) Development of a novel parallel double-stage yielding buckling restrained brace: Theoretical, experimental, and numerical investigations. *J Build Eng* 68:106089
- Zhao J, Lin F, Wang Z (2016) Effect of non-moment braced frame seismic deformations on buckling-restrained brace end connection behavior: theoretical analysis and subassemblage tests. *Earthq Eng Struct Dynam* 45(3):359–381
- Zhao H, Shi G, Gao Y (2023) Experimental study on cyclic behavior of low yield point steel buckling-restrained braces. *Eng Struct* 277:115464
- Zhou Y, Shao H, Cao Y, Lui EM (2021) Application of buckling-restrained braces to earthquake-resistant design of buildings: a review. *Eng Struct* 246:112991

Springer Nature or its licensor (e.g. a society or other partner) holds exclusive rights to this article under a publishing agreement with the author(s) or other rightsholder(s); author self-archiving of the accepted manuscript version of this article is solely governed by the terms of such publishing agreement and applicable law.